electronics

Article

Aging Characteristics and State-of-Health Estimation of Retired Batteries: An Electrochemical Impedance Spectroscopy Perspective

Ziyong Xu [1,2], He Li [2], Mohammad Yazdi [2], Konglei Ouyang [2,*] and Weiwen Peng [2]

[1] Bangor College China, Central South University of Forestry and Technology, Changsha 410004, China
[2] School of Intelligent Systems Engineering, Shenzhen Campus of Sun Yat-sen University, Shenzhen 518107, China
* Correspondence: ouyklei@mail2.sysu.edu.cn

Abstract: In this paper, the aging characteristics and state-of-health (SOH) estimation of retired batteries were studied by leveraging the electrochemical impedance spectroscopy (EIS) technique. A battery aging experiment was designed and implemented to monitor the aging process of batteries, after which a comprehensive analysis of the collected EIS data was conducted to characterize the corresponding aging properties of retired batteries. Based on the aging data analysis results, an equivalent circuit model (ECM) was constructed, and the correlation between ECM parameters and the battery age was identified. An EIS-based and ECM-based SOH estimation method for retired batteries was developed and demonstrated. Furthermore, to further leveraging the EIS data from battery aging tests, a Bayesian neural network-based SOH estimation method with automatic feature extraction was developed. Comparisons among the proposed model-based method, data-driven method, and state-of-the-art SOH estimation method for retired batteries were implemented. Overall, insights into the aging characteristics and SOH estimation of retired batteries were achieved by leveraging the EIS technique.

Keywords: retired battery; state of health; electrochemical impedance spectroscopy; data-driven method

Citation: Xu, Z.; Li, H.; Yazdi, M.; Ouyang, K.; Peng, W. Aging Characteristics and State-of-Health Estimation of Retired Batteries: An Electrochemical Impedance Spectroscopy Perspective. *Electronics* **2022**, *11*, 3863. https://doi.org/10.3390/electronics11233863

Academic Editor: Bor-Ren Lin

Received: 16 October 2022
Accepted: 16 November 2022
Published: 23 November 2022

1. Introduction

The rapid development of electric vehicles in recent years has led to wide applications of lithium-ion batteries [1]. It is expected that by 2025, the retired lithium-ion batteries from electric vehicles will be more than one million tons [2,3]. Retired batteries from electric vehicles usually retain 70–80% of their initial capacity [3]. Thus, serious environmental pollution and massive waste of resources might happen if these huge amounts of retired lithium-ion batteries are not properly handled. Second-life applications of retired batteries, such as energy storage systems (ESSs), communication base stations, low-speed electric vehicles, and other scenarios that require lower performance than electric vehicles, are becoming promising ways for handling retired batteries environmentally and economically. To adequately recycle retired batteries through these second-life applications, one critical issue is to characterize the aging pattern and to further implement the precise state-of-health (SOH) estimation of retired batteries [4].

The SOH of a retired battery is a measurement of the performance of an aged battery in its current state [5]. Usually, the SOH is evaluated using the remaining capacity of the battery. Aging and improper operation affect the performance of batteries, and the possibility of a catastrophic accident increases after the performance drops to a certain level [6]. Retired batteries have the characteristics of low energy density, low power, and poor consistency. Comprehensive health monitoring is essential for engineering facilities [7–12], such as batteries [13], which can ensure the rational, safe, and efficient use of retired power batteries. Based on health monitoring, a precise SOH estimation method for retired batteries that relies on constructing an accurate relationship between fast battery test data and the current SOH can be constructed. There are generally three ways for developing a precise SOH estimation method [14,15]: electrochemical-model-based, equivalent-circuit-model-based, and data-driven methods.

The electrochemical model characterizes the chemical reaction processes in the battery, such as solid-state diffusion, liquid-phase diffusion, and migration processes [16]. This model can provide a complete description of the reaction mechanism of the battery. It consists of a series of partial differential equations for electrode and electrolyte kinetics, which are highly accurate but computationally intensive [17]. The dominant electrochemical model is the Pseudo Two-Dimensional (P2D) model [18], based on porous electrodes and concentrated solution theory [19]. The P2D model is complex, and its simplified Single-Particle Model (SPM) [20] has the advantage of low computational effort. In summary, electrochemical models can reflect the changes in internal parameters corresponding to battery performance degradation. However, due to their complex model construction process, the difficulty in obtaining accurate internal battery parameters, and the complexity of calculations, they are generally used for failure mode analyses of batteries to aid design and development.

The equivalent circuit model (ECM) adopts circuit components, such as constant voltage sources, resistors, inductors, capacitors, etc., to characterize the charging and discharging properties of batteries [21]. The ECM captures the current–voltage (I-V) characteristics and transient behavior of the battery by approximating the dynamic characteristics of batteries. ECMs are semi-mechanical models and are subdivided into two categories [22]: frequency-domain models and time-domain models. The time-domain models are generally based on the I-V response data of the battery, and the frequency-domain models are generally based on electrochemical impedance spectroscopy (EIS) data [23]. ECMs include the resistor–capacitor network model [24], the nonlinear ECM [25], and the Thevenin model [26]. Time-domain models are more computationally friendly for practical applications, while frequency-domain models can analyze the electrochemical impedance formed by different factors inside the battery in a broader frequency domain with relatively high accuracy. Although the ECM simplifies model complexity, it is difficult to build models to reflect the dynamic health characteristics of batteries due to the complexity of their internal principles and the uncertainty of their operating conditions. It is difficult to fit the same ECM to different types of batteries due to the significant variability of the internal parameters of each type of battery, which limits the scalability of ECM-based methods for SOH estimation models for different types of batteries.

The data-driven approach directly extracts the health-related features associated with battery aging, avoiding the need for complex electrochemical process analyses and model construction. Data sources for data-driven methods can be multi-faceted test data, including charge and discharge data, EIS test data, etc. In recent years, powerful machine learning algorithms have been used to train offline data and estimate the SOH of batteries. Jiang et al. [27] proposed an SOH estimation method for the cascade utilization of retired $LiFePO_4$ batteries based on incremental capacity (IC) curves and ridge regression. Six retired $LiFePO_4$ batteries were selected for run-to-failure testing in three typical loading modes for energy storage applications, and the characteristics of the IC curves were used as inputs to the regression model. The final SOH estimation error was within 3%. Peng et al. [28] proposed a data-driven model to predict Li-ion batteries' performance degradation behavior and to estimate the SOH. The comparison with existing methods confirmed that the combined algorithm of Gaussian Process Regression (GPR) and extended Kalman filter (EKF) showed higher accuracy than other algorithms. Li et al.'s [29] paper proposed a novel SOH estimation model based on Catboost and interval capacity during charging processes, with which a general aging feature of the interval capacity was extracted using incremental capacity analyses. The results showed that the error of the estimation was limited within 2.74% and was better than five existing data-driven models.

Due to the lack of aging data of retired batteries in second-life applications, few studies have been reported on the analysis of the aging characteristics and the investigation of an SOH estimation method for retired batteries. As reviewed above, most existing approaches use equivalent circuit models to describe the aging behavior of battery systems and further develop SOH estimation models based on ECM parameter identification. However, changing battery types, operating conditions, and test conditions can challenge the applicability of this ECM parameter identification, which is one of the limitations of EIS practicality.

To fill these gaps, this paper is devoted to the experimental study of the cycle aging of retired batteries and to the thorough investigation of model-based and data-driven methods for the SOH estimation of retired batteries. Compared with the conventional perspective on battery aging studied through current and voltage measurements, this paper presents a novel EIS perspective for the study on the aging characterization and the SOH estimation of retired batteries. This EIS perspective is elaborated mainly with the consideration that EIS measurements contain richer information about batteries, including materials, interfacial phenomena, and electrochemical reactions, making it easier to understand the battery aging process mechanistically. One major challenge of this EIS perspective lies in the fact that it is challenging to identify the quantitative characteristics associated with battery aging over such a wide range of frequencies (the range of 0.01–5000 Hz was recorded in this paper). To handle this challenge, Bayesian neural network-based SOH estimation with automatic feature extraction was developed. This automatic feature extraction can automatically identify useful EIS features from a wide range of frequencies. In addition, the uncertainty quantification of SOH estimation in the DL-based method can be obtained through the proposed Bayesian neural network-based method. This uncertainty quantification is often omitted in traditional deep learning-based SOH estimation methods, yet it is critical for uncertainty-aware decision making for the safe operation of retired batteries.

Based on the above, the novel contributions of this paper are the following:

(1) To present a novel EIS perspective for the study of the aging characteristics of and SOH estimation method for retired batteries, which provides an understanding of the battery aging process mechanistically.
(2) To develop Bayesian neural network-based SOH estimation with automatic feature extraction to identify the quantitative characteristics associated with battery aging over a wide range of frequencies.

The rest of the paper is organized as follows: Section 2 describes the experimental study of battery aging. Section 3 introduces the proposed EIS-based SOH estimation method. Section 4 demonstrates the proposed SOH estimation method based on the aging data from the experiments. Section 5 concludes the paper with a discussion.

2. Experimental Setting and Data Acquisition

2.1. Life-Cycle Aging Experiment

This section firstly introduces the principles of electrochemical impedance spectroscopy measurements and clarifies the settings of the EIS test. Secondly, we report the process for building an experimental platform for the experiment. Finally, we report the design of the life-cycle aging experiments on batteries.

(1) **Electrochemical Impedance Spectroscopy**

Electrochemical impedance spectroscopy (EIS) [30] is an essential electrochemical test method. EIS maps the change in the electrochemical frequency due to a small AC excitation signal according to the sinusoidal law with the cell in equilibrium (open-circuit condition) or under a stable DC polarization condition, called frequency-domain impedance analysis [31]. On the other hand, the time-domain impedance analysis measures the variation in the AC impedance with time at a fixed frequency [32].

As a non-linear and time-varying electrochemical system, the prerequisites for the impedance measurements of Li-ion batteries should satisfy the causality, linearity, and stability conditions [33]. To satisfy these conditions, batteries should be in non-operating equilibrium during measurements, and the amplitude of the potential sine wave, usually used as a disturbance signal, is to be set at 5–10 mV [30–34]. The AC impedance can be measured in constant current or potential mode. The constant potential mode can lead to overcurrent under the low impedance of batteries. Electrical impedance is the measure of the opposition that a circuit presents to a current when a voltage is applied. The impedance in the frequency domain can be calculated from the perturbed signal and its response, that is,

$$Z = \frac{u}{i} = \frac{U \cdot \sin(\omega t + \phi_u)}{I \cdot \sin(\omega t + \phi_i)} \tag{1}$$

where U U is the amplitude of the voltage signal, I is the amplitude of the current signal, w is the angular frequency, and ϕu and ϕi are the phase shifts.

Accordingly, the absolute value of the impedance ($|Z|$) and phase shift (ϕ) are obtained by solving

$$|Z| = \frac{U}{I} \tag{2}$$

$$\phi = \phi_u - \phi_i \tag{3}$$

The impedance can be further given as follow,

$$Z = Zre + jZim \tag{4}$$

where Zre is the real part of the impedance and Zim is the imaginary part of impedance.

Figure 1 visualizes the interrelationship among the EIS measurement parameters. Using the real part of the impedance as the horizontal coordinate and the negative imaginary part as the vertical coordinate, the Nyquist plot shows the cell impedance at different frequencies, from left to right, corresponding to high and low frequencies, as shown in Figure 2.

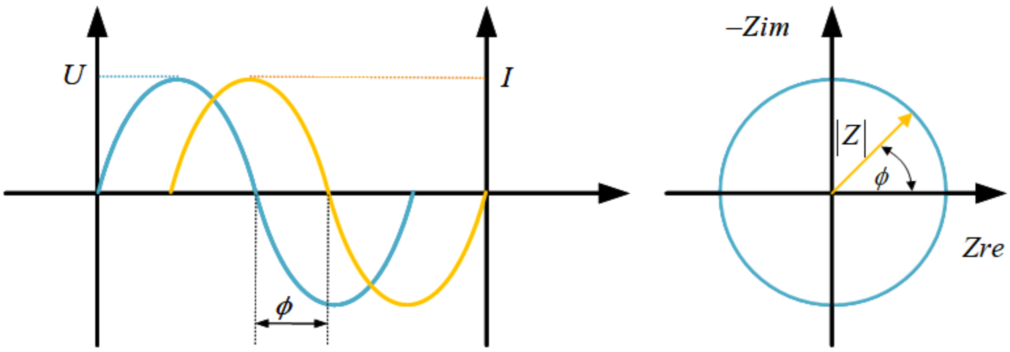

Figure 1. Analysis of EIS measurement principles.

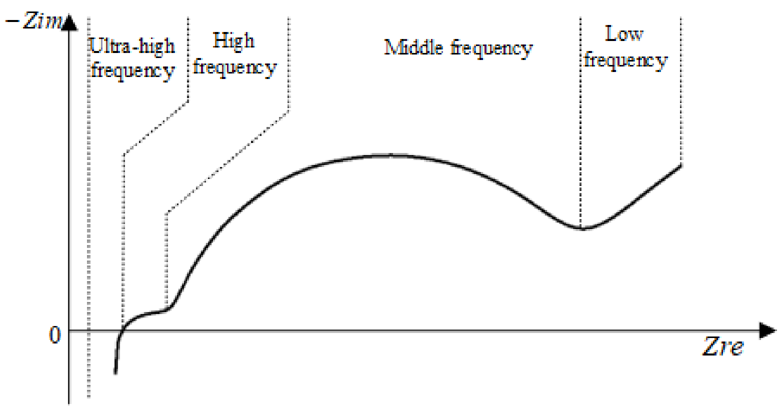

Figure 2. Electrochemical impedance spectrum of lithium-ion battery.

(2) **Experimental Setting**

The experimental platform (Figure 3) in this study consisted of a battery charge/discharge test system (NEWARE BTS-5V12A), a multi-channel electrochemical workstation (Solartron analytical 1470E), a computer with NEWARE-BTS test software and Solartro-Cell Test software installed, and a thermostat (KOMEG KMT-150G). The battery charge/discharge test system was used for charge/discharge cycles, capacity calibration, HPPC testing, etc. The I-V data were collected during the charge/discharge process. The electrochemical workstation was used to measure the EIS spectrum of the battery. The frequency, the real part of impedance, the imaginary part of the impedance, and several other types of data were recorded. The maximum AC impedance frequency range was 10 μ Hz ~ 1 MHz; the frequency analysis accuracy amplitude was 0.1% of the phase angle. NEWARE-BTS test and Solartron-Cell Test software recorded and exported the test data to the computer. The thermostatic chamber provided all test ambient temperatures in the range of −20 °C to 180 °C, with a temperature fluctuation of ±0.5 °C. Eight cylindrical lithium-ion batteries (18650-NCM523) were tested, with labels Cell-1 to Cell-8 (Table 1).

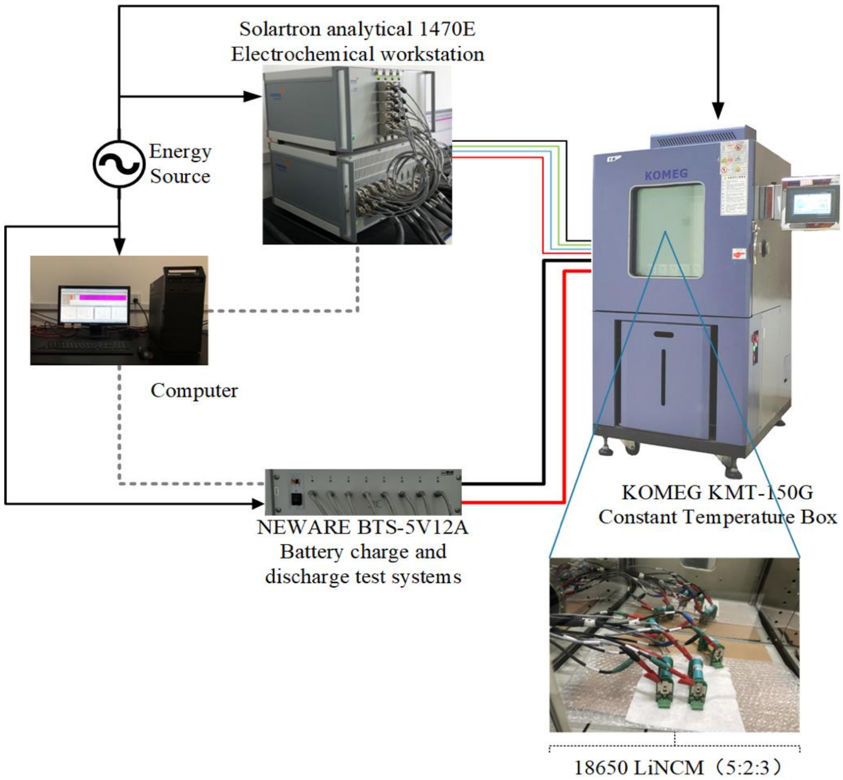

Figure 3. The experimental platform for the batteries.

Table 1. Parameters of the tested batteries.

Item	Parameter	Item	Parameter
Negative electrode material	Artificial graphite	Capacity	2000 mAh
Size	Diameter, 18.6 mm; height, 65.3 mm	Voltage	3.6 V
Positive electrode material	$Li(Ni_{0.5}Mn_{0.3}Co_{0.2})O_2$	Discharge cut-off voltage	2.75 V
Weight	43 g	Charge cut-off voltage	4.20 ± 0.05 V

(3) **Experimental flowchart**

Based on the above-described experimental platform, this section reports the design of a life-cycle aging test process for the batteries (LiNCM) (Figure 4). The test included two major stages: the accelerated aging test for vehicle applications and the test for typical energy storage scenarios. The aging cycle conditions used in the two stages were different, but the performance evaluation of the battery was the same, that is, every 50 cycles. Battery performance testing consisted of capacity calibration, HPPC, and EIS. At the end of the first stage of the battery life, the maximum remaining usable capacity was less than 80% of the nominal capacity, which was in line with the power-cell retirement criteria (70–80% of initial capacity). At the end of the second stage of the battery life, the maximum remaining usable capacity of all batteries tested was less than 60% of nominal capacity, which met the EOL criteria for the relevant decommissioning power-cell storage scenario.

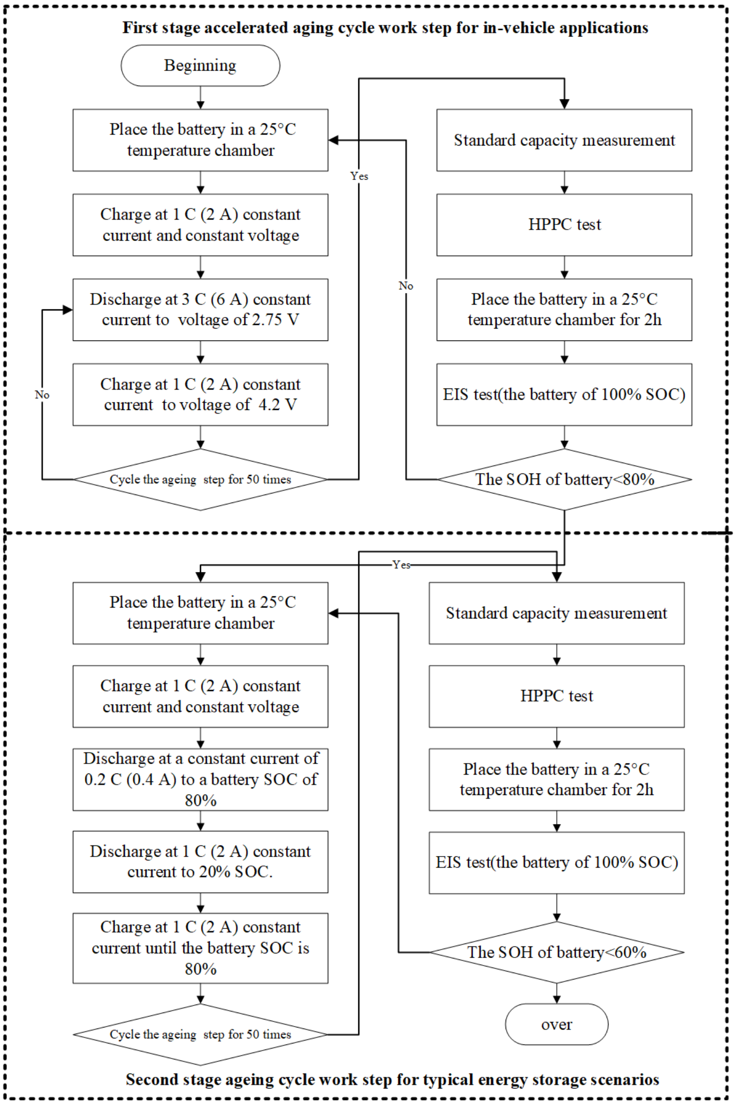

Figure 4. Flow chart of the life-cycle aging experiment.

The life-cycle battery aging experiment was conducted as shown below.

(1) Accelerated aging cycle work step for in-vehicle applications

In order to accelerate the aging rate in the first stage, the cyclic aging conditions were set to be 0–100% of the battery state of charge (SOC), 1 C constant current and voltage charge, and 3 C constant current discharge. The specific operations were:

- Preserve the battery at 25 °C for 60 min.
- Charge at 1 C (2 A) until the cut-off voltage of 4.2 V and the current of 0.02 C (0.04 A) are achieved.
- Preserve for 30 min.
- Discharge at 3 C (6 A) constant current until the cut-off voltage of 2.75 V is achieved.
- Preserve for 60 min.

- Charge at 1 C (2 A) until the cut-off voltage of 4.2 V and the current of 0.1 C (0.2 A) are achieved.
- Repeat the first three steps until 50 cycles are completed.

We conducted the performance test every 50 cycles, including capacity calibration, HPPC, and EIS tests.

(2) Aging cycle for typical energy storage scenarios

The aging cycle condition refers to the cycle test method in GB36276-2018 (Li-ion Battery for Power Storage), and the cycle aging conditions were 20–80% of the SOC interval for 1 C constant current charging/discharging. The specific steps were as follows:

- Preserve the battery at 25 °C for 60 min.
- Charge at 1 C (2 A) until the cut-off voltage of 4.2 V and the current of 0.02 C (0.04 A) are achieved.
- Preserve for 10 min.
- Discharge at the constant current of 0.2 C (0.4 A) to 80% SOC.
- Preserve for 5 min.
- Discharge at the constant current of 1 C (2 A) to 20% SOC.
- Preserve for 30 min.
- Charge at the constant current of 1 C (2 A) until 80% SOC.
- Preserve for 30 min.
- Repeat the last four steps until 50 cycles are completed.

We conducted the performance test every 50 cycles, including capacity calibration, HPPC, and EIS tests.

(3) Capacity calibration test

The capacity calibration test aimed to obtain the maximum remaining available capacity of batteries. To make sure the efficiency and accuracy of capacity measurements, the capacity calibration test adopted the following steps:

- Preserve the battery at 25 °C for 60 min.
- Charge at 1 C (2 A) until the cut-off voltage of 4.2 V and the current of 0.02 C (0.04 A) are achieved.
- Preserve for 10 min.
- Discharge at the constant current of 1C (2A) until the cut-off voltage of 2.75 V is achieved.
- Preserve for 10 min.
- Discharge at the constant current of 0.05 C (0.1 A) with a cut-off voltage of 2.75 V.
- Preserve for 5 min.
- Charge at the constant current 1 C (2 A) until the cut-off voltage of 4.2 V and the current of 0.02 C (0.04 A) are achieved.

The battery final maximum usable discharge capacity corresponded to the sum of the two discharges in steps 4 and 5, and the maximum remaining usable charge capacity corresponded to the constant current and voltage charge capacity in step 8.

2.2. Data Acquisition and Analysis

This paper presents charge and discharge cycle data, capacity calibration test data, HPPC test data, and EIS test data of the batteries tested. The changes in the capacity decay and internal resistance of the batteries over the life cycle were calculated, and the aging pattern of the battery under the two cycling conditions was analyzed from the perspective of external characteristics. An ECM was established based on EIS test data, and the changes in the impedance of each part of the battery during aging were modeled.

(1) Experimental Data Analysis of External Characteristics

The degradation of the battery capacity reduces the maximum available capacity, and the increase in internal resistance leads to the degradation of the battery power. This study assessed the state of battery degradation by studying the capacity.

Capacity decay

The refinement index of a battery nominal capacity includes the Maximum Rechargeable Capacity (MRC) and the Maximum Dischargeable Capacity (MDC). The average values of MRC and MDC are used to calculate the nominal capacity. Moreover, the depth of discharge (DOD) is the percentage of battery discharge capacity and battery rated capacity. The capacity degradation curves of all tested batteries as presented in this chapter are shown in Figure 5. The following conclusions were drawn:

- The first stage of capacity degradation of the batteries could be divided into the following: cycles 0–50, in which the capacity of all new power batteries had a slight increase; cycles 50–500, which was the linear aging stage (i.e., the capacity degradation of all batteries increased linearly with the number of cycles), in which the capacity degradation curves of the batteries were close; and cycles 500–1000, which was the non-linear aging stage. All batteries showed a significant increase in the capacity decay rate, and the capacity decay curves of the batteries in this stage became increasingly scattered, indicating that the inconsistency among the batteries increased significantly. The standard deviation was 95.13 mAh.
- After 1000 cycles, there was a significant increase in battery capacity. This was a self-recovery phenomenon caused by the batteries being left for two months between the end of the first phase of testing and the start of the second phase of cycling. More significant battery self-recovery also occurred at the 2100th and 2400th cycles.
- The capacity decay rate in the second battery life stage was slower than that in the first life stage. In addition, there was no apparent non-linear inflection point in the capacity decay curve in the second stage, which showed a linear degradation trend. In terms of inter-cell variability, the inter-cell inconsistency at the point when second-life-stage testing stopped (2700 cycles) was lower than the first-stage cut-off, as demonstrated by the extreme inter-cell capacity difference of 172.4 mAh, with a standard deviation of 57.06 mAh.

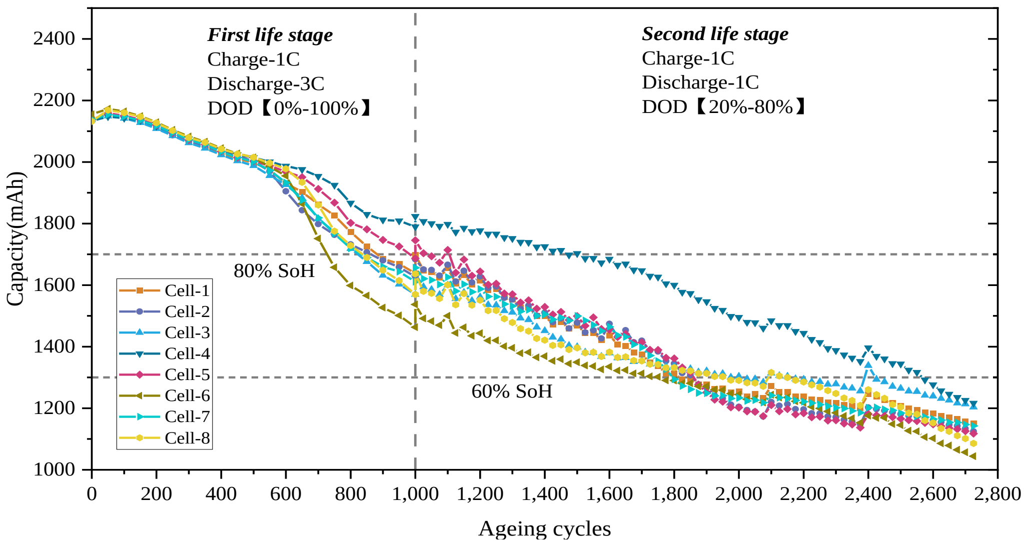

Figure 5. Life–capacity decay curve of the tested cells. Capacity (mAh).

(2) **Electrochemical Impedance Spectroscopy Analysis**

The EIS tests were conducted at 20 °C in a non-operating steady state with a battery SOC of 100%. The KK (Kramers–Kronig) transformation method [35] was used to show the EIS test data. Figure 6 indicates that the measured impedance spectrum fitted the KK-fitted reconstructed values, with the maximum residuals for both the real and imaginary parts being within 0.5%. Therefore, it was concluded that the EIS data for these measurements satisfied the KK relationship.

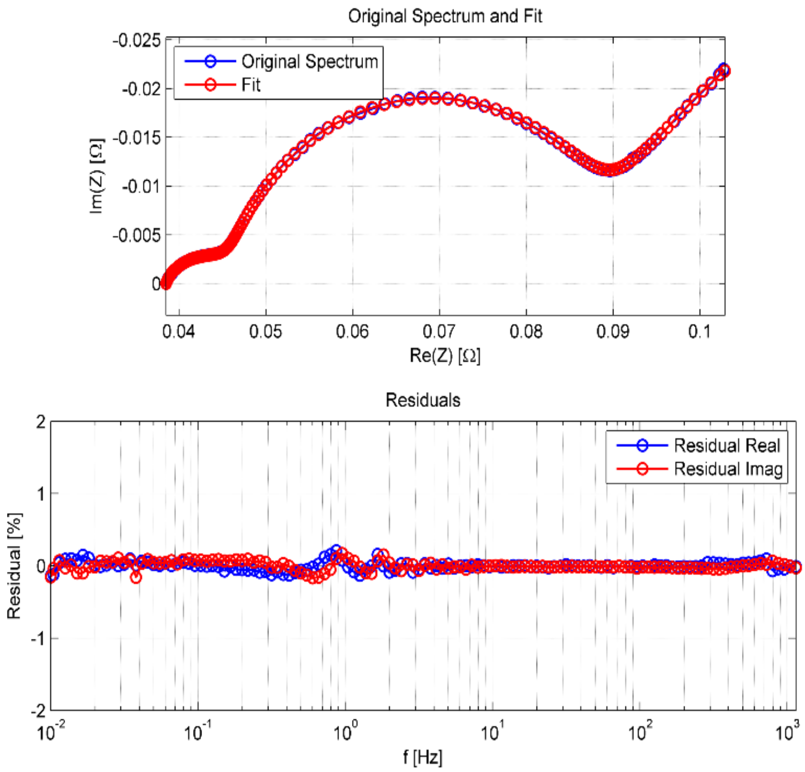

Figure 6. Electrochemical impedance spectra and their KK transformation test results.

The first-life-stage EIS profiles of the test cell (Cell-1) in this chapter and the second-life-stage EIS profiles of all cells are shown in Figures 7 and 8, respectively. As the EIS tests are influenced by the cell temperature and SOC, the tests referred to in the figures were all performed at 20 °C and 100% SOC. The difference between the two stages of EIS testing lay in the different frequency bands, with first-life-stage testing being performed at 0.1–5000 Hz and second-life-stage testing being performed at 0.01–5000 Hz. As shown in Figures 7 and 8, the EIS of the battery changed regularly with the increase in the cycle times, indicating a correlation among EIS, battery capacity degradation, and other performance degradation; combined with the impedance model, this could be used to establish a link between the internal parameters of the battery during cyclic aging and thus to characterize the health status of the battery.

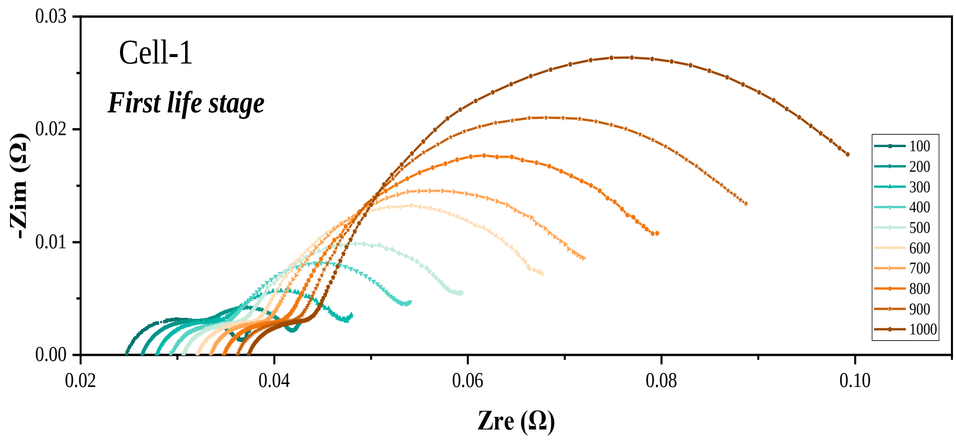

Figure 7. EIS mapping of the first life stage of the test cell (Cell-1).

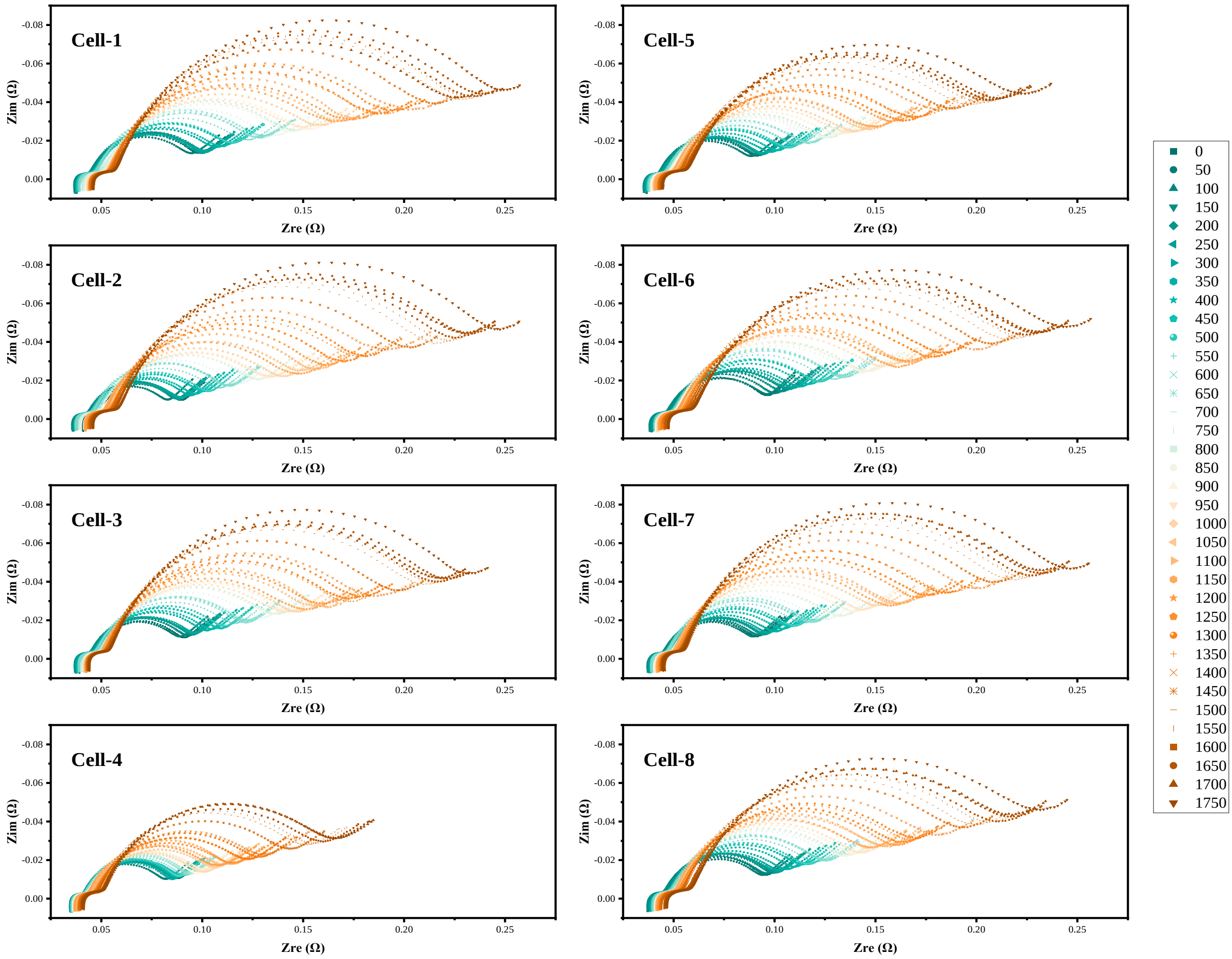

Figure 8. Nyquist diagrams for the second life stage of the test cells at different cycles.

In Figures 7 and 8, different colors and symbols represent the Nyquist diagrams of the batteries at different cycles, low frequencies to high frequencies are represented from left to right. This comment is valid for other similar figures.

According to Figures 7 and 8, the following conclusions could be drawn:

- As the number of aging cycles increased, the associated EIS spectrum of the battery moves from the left to right as shown the figures. The intersection of the EIS spectrum with the coordinate axis where the fundamental part of the impedance is located indicated the internal ohmic resistance, and the shift in the EIS spectrum to the right indicated the increase in the internal ohmic resistance during the battery aging process.
- In the early stages of aging (100 cycles), the EIS spectrum behaved as semi-circular arcs in the mid-frequency band, and as the number of cycles increased, two arcs separated at 19.9 Hz, as shown in Figure 9. During subsequent cell aging, the size of the first segment arc did not change significantly, while the radius of the second segment arc increased significantly. As the cell aged, the impedance spectrum high-frequency-band arcs remained largely inconvenient due to the stability of the solid electrolyte interphase (SEI) film on the anode active ion surface. It should be noted that the SEI layer was not stable under all conditions and was highly susceptible to rupture and decomposition under high-temperature and high-magnification operating conditions. As the number of aging cycles increased, the impedance spectrum increased significantly in the low-frequency band arc, which indicated an increase in the internal charge transfer impedance of the cell. This increase of impedance spectrum at the end of the first stage of aging cycles was mainly related to the impedance of the cathode.

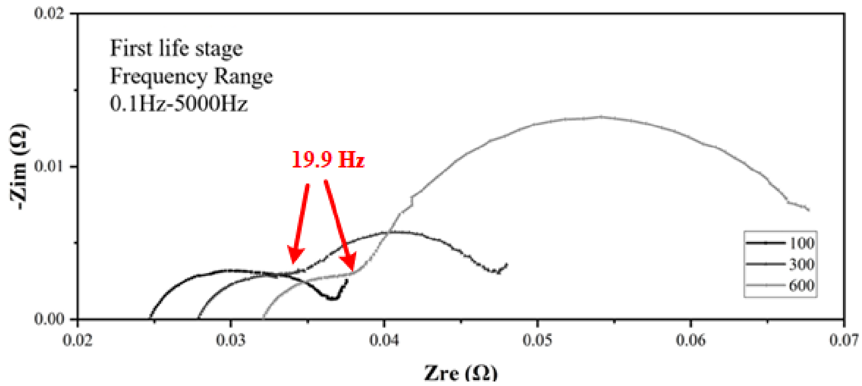

Figure 9. Separation points of the impedance spectrum semicircles.

The variation in the EIS spectrum with the cycles in Figure 10 indicates the following:

- In the early stage of recycling the retired battery, the EIS spectrum clearly showed two semicircles in the middle-frequency band because the retired battery formed a stable SEI layer after the long period of the first stage of cycling.
- During the recirculation of the retired battery, the radius of the first semicircle was almost maintained, and the radius of the second semicircle increased significantly.
- The EIS curve decreased in the sloping part of the low-frequency band with the increase in the number of cycles, representing that the diffusion capacity of lithium ions decreased with battery aging and that the diffusion coefficient of lithium ions decreased.

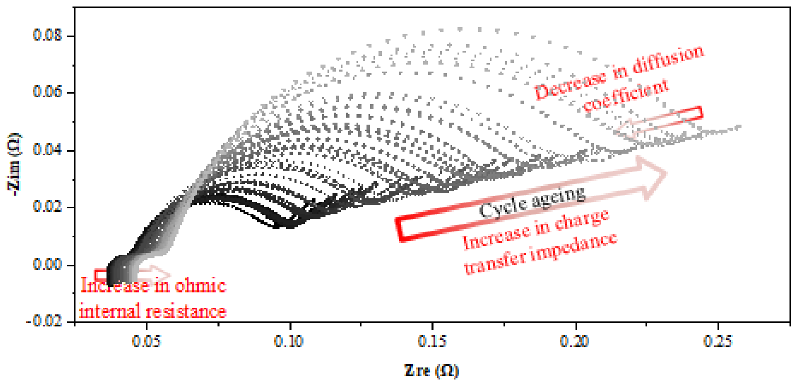

Figure 10. Cyclic aging Nyquist plot of batteries.

3. The Proposed Method

3.1. EIS-Based SOH Estimation

The EIS-based SOH estimation method for retired batteries is shown in Figure 11. The framework is divided into two technical lines, one based on the electrochemical impedance spectroscopy ECM parameter identification method and the other based on the automatic relevance determination (ARD) algorithm. The specific implementation process was performed as follows:

- Feature extraction: Firstly, the EIS data collected during the operation of the retired power battery were used to build a dataset; then, a suitable equivalent circuit model was established to describe the electrochemical process of the battery based on the feature extraction of the ECM method, and the parameters in the ECM were identified using an optimization algorithm. The appropriate parameters were selected for SOH estimation; the ARD algorithm was used to calculate the weights and the feature pruning of the EIS frequency features to obtain the de-modeled features; finally, the feature frequency most relevant to the battery capacity was selected, and the real and imaginary parts of the impedance at the feature frequency could be used as the feature dataset for SOH estimation.

- Model building and training: Firstly, the feature dataset was divided into a training set and a test set using division methods such as random division and leave-one-out cross-validation division. Secondly, the BNN model was built based on the Bayesian deep learning framework. Afterwards, the training dataset was input into the BNN, and due to the problem that it was difficult to calculate the posterior distribution during the learning process of the BNN model, variational inference was used to use a processable variational distribution to approximate the posterior distribution, transforming standard Bayesian learning from an integration problem to an optimization problem. Finally, the hyperparameters of the BNN were optimized to improve the performance and effectiveness of model learning.
- Estimation of the health status: The SOH of the retired batteries was estimated by feeding the test dataset into the BNN model obtained from training. Random division and leave-one-out methods were used to divide the test set so that the model performance on anonymous data could be tested more comprehensively. The SOH estimation error was calculated based on the SOH estimates output by the model and the real, measured SOH. The RMSE and MAPE were used to assess the accuracy and generalization performance of the model.

3.2. Feature Extraction Based on ECM Parameter Identification

EIS-based methods for battery SOH estimation require understanding battery aging in conjunction with the ECM and identifying health features from ECM-identified parameters that are highly correlated with the SOH. In this section, we report the process with which the parameters of the ECM built for the test batteries were first identified and with which the health features were extracted from the ECM parameters after a correlation analysis.

(1) **ECM construction and parameter identification**

The relationship between the battery SOH and characteristics of the EIS spectra was further investigated by fitting the EIS spectra to the ECM, and the second-order ECM is shown in Figure 12. In Figure 12, L represents the ideal inductance for the impedance behavior of the cell at very high frequencies, and RO represents ohmic impedance. The electrochemical process at the electrode is represented by the modified parallel RC elements, $Zarc$ and ZW. $Zarc$ introduces a constant phase element; Q_{CPE} represents a capacitor in parallel with a standard resistor to account for the dispersion effect; Z_{arc1} is used to describe the impedance of SEI; Z_{arc2} is used to describe the charge transfer impedance. The properties of ZW are similar to those of parallel RC elements and are used to describe the diffusion impedance of lithium ions in the solid particles of the electrode.

Specifically, $Zarc$ is expressed by the following:

$$Z_{arc}(\omega) = Z_R//Z_{CPE} = \frac{1}{1/R + \theta(j\omega)^n} \tag{5}$$

where n is a depression factor, is valid between 0 and 1, and is used to simulate the depression of the semicircle in the Nyquist diagram. When n is equal to 0, $Zarc$ is the ohmic resistor; when n is equal to 1, it represents the RC component's perfect semicircle. ZW is expressed as follows:

$$Z_W = R\frac{\tanh(\sqrt{j\omega\theta})}{\sqrt{j\omega\theta}} \tag{6}$$

Commonly, Z_W is approximated as $\frac{R_W}{(j\omega)^{0.5}}$.

The total impedance of the equivalent circuit model in Figure 12 can be described as follows:

$$\underline{Z} = R_O + \frac{R_{SEI}}{1 + R_{SEI} \cdot \theta_1(j\omega)^{n_1}} + \frac{R_{ct}}{1 + R_{ct} \cdot \theta_2(j\omega)^{n_2}} + \frac{R_W}{(j\omega)^{0.5}} \tag{7}$$

where $\underline{Z}$ is the total impedance.

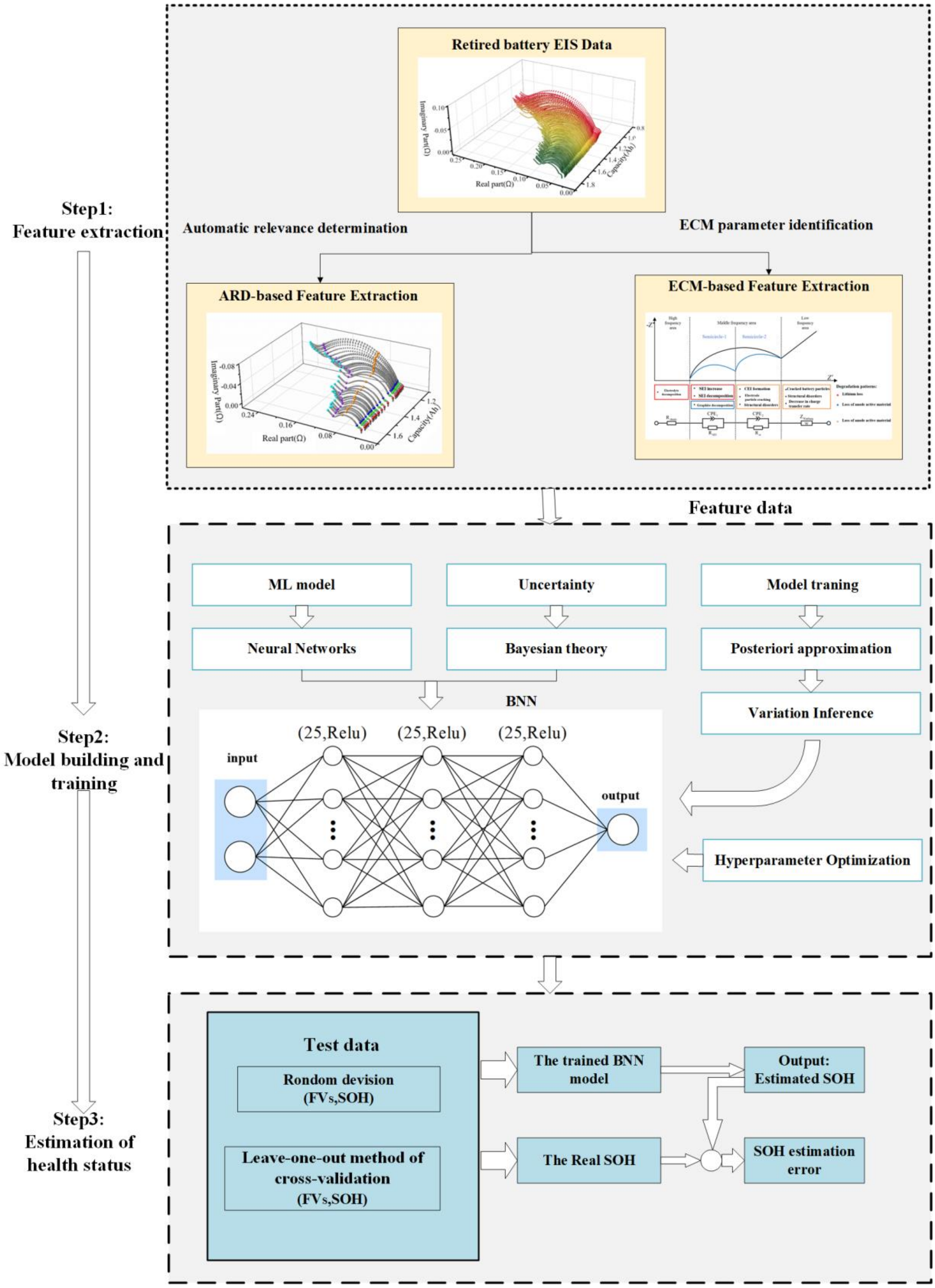

Figure 11. Research Framework of SOH Estimation Method for Decommissioned Batteries Based on CC-CV Charge Data and BNNs.

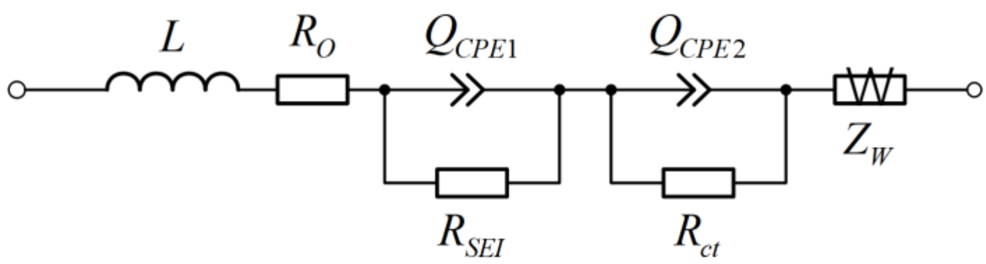

Figure 12. Second-order equivalent-circuit-model structure.

The expressions for the real (Zre) and imaginary (Zim) parts of the total impedance are derived as follows:

$$Zre = R_O + \frac{R_{SEI}+\theta_1 R_{SEI}{}^2\omega^{n_1}\cos\left(\frac{n_1\pi}{2}\right)}{\left[Y_1 R_{SEI}\omega^{n_1}+\cos\left(\frac{n_1\pi}{2}\right)\right]^2+\sin^2\left(\frac{n_1\pi}{2}\right)} + \frac{R_{ct}+\theta_2 R_{ct}{}^2\omega^{n_2}\cos\left(\frac{n_2\pi}{2}\right)}{\left[\theta_2 R_{ct}\omega^{n_2}+\cos\left(\frac{n_2\pi}{2}\right)\right]^2+\sin^2\left(\frac{n_2\pi}{2}\right)} \tag{8}$$

$$Zim = \omega L - \frac{\theta_1 R_{SEI}{}^2\omega^{n_1}\sin\left(\frac{n_1\pi}{2}\right)}{\left[\theta_1 R_{SEI}\omega^{n_1}+\cos\left(\frac{n_1\pi}{2}\right)\right]^2+\sin^2\left(\frac{n_1\pi}{2}\right)} - \frac{\theta_2 R_{ct}{}^2\omega^{n_2}\sin\left(\frac{n_2\pi}{2}\right)}{\left[\theta_2 R_{ct}\omega^{n_2}+\cos\left(\frac{n_2\pi}{2}\right)\right]^2+\sin^2\left(\frac{n_2\pi}{2}\right)} \tag{9}$$

The impedance spectrum is parametrically identified using the non-linear least square method with an optimization objective function.

$$\begin{cases} f(\lambda) = \sum\limits_{i=1}^{k}\left((Zre_i - zre_i)^2 + (Zim_i - zim_i)^2\right) \\ \lambda = [L, R_O, R_{SEI}, \theta_1, n_1, R_{ct}, \theta_2, n_2, R_W] \end{cases} \tag{10}$$

where k is the total number of impedances at all frequency points on the impedance spectrum; Zre_i and Zim_i are the actual values of the measured real and imaginary parts of the impedance at a given frequency; Zre_i and Zim_i are the fitted values of the real and imaginary parts of the impedance measured at a specific frequency; and λ is a vector of unknown parameters. In this study, a total of 280 measured impedance spectra from the second life stage of retired power cells were fitted to identify nine parameters of the ECM $(L, R_O, R_{SEI}, \theta_1, n_1, R_{ct}, \theta_2, n_2, R_W)$. The measured EIS susceptibility component does not provide valid battery health information; it is, therefore, outside the scope of this characterization study.

(2) **ECM parameter analysis and feature extraction**

The parameter identification for the ECM of the EIS spectrum was carried out using the non-linear least square method, and the error control of the ECM parameter identification in this study was 10%. From the Spearman correlation between ECM parameters and the capacity as shown in Table 2, we can find that R_O and R_W show a robust correlation with cpacity. Thus, we chose R_O and R_W for the battery health-state estimate characteristics. The trends of R_W and R_O are shown in Figure 13.

Table 2. Spearman correlation between ECM parameters and capacity.

Parameter	Correlation Coefficient	Parameter	Correlation Coefficient
R_O	−0.9238	R_{ct}	0.2353
R_{SEI}	−0.5903	θ_2	0.6209
θ_1	0.2711	R_W	0.9696

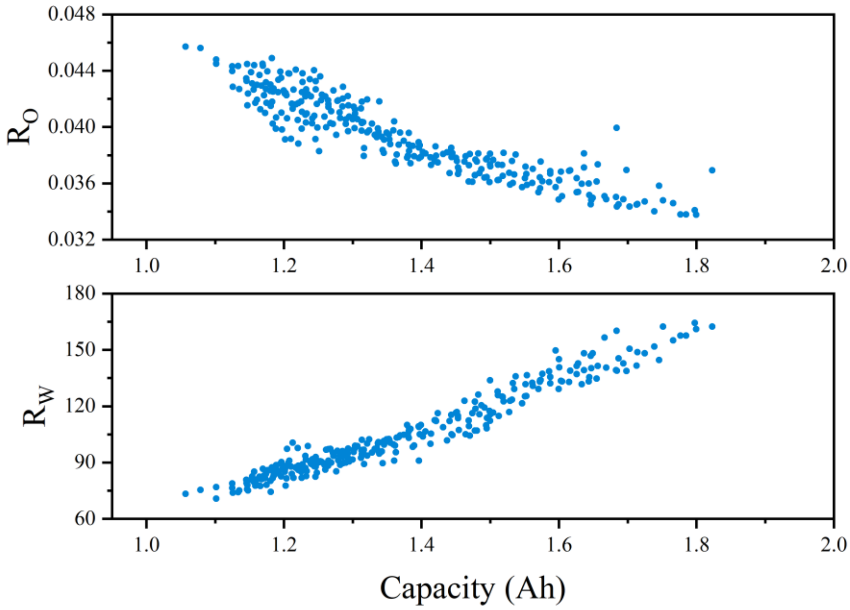

Figure 13. Relationships between ECM parameters and battery capacity.

(3) **ARD-based Automated feature extraction**

Considering the difficulty in selecting suitable feature frequencies using current EIS-based, data-driven methods, this study used the automatic relevance determination (ARD) algorithm to automate the selection of health factors associated with battery aging from the EIS spectra, avoiding the need for complex electrochemical process analyses and model construction. In practical regression problems, the inputs contain many potentially uncorrelated features. Automatic correlation decision making is a Bayesian approach based on feature selection and sparse learning [36]. The relevance hyperparameters in the ARD algorithm determine the range of the variation in the parameters associated with a particular input. The relevance of the input parameters to the prediction outcome is inferred by modeling the width of a zero-mean Gaussian distribution before these parameters. ARD maximum likelihood optimizes the hyperparameters to infer the relative importance of the inputs.

The idea of ARD is to give feature weights that are independent of the Gaussian prior.

$$p(w \mid \alpha) = \prod_i \mathcal{N}\left(w_i \mid 0, \alpha_i^{-1}\right) \tag{11}$$

where α is a hyperparameter vector that controls how far each weight is allowed to deviate from zero. The hyperparameter α can be estimated by using the expectation maximization (EM) method or Bayesian method with maximum a posteriori probability estimate (MAP). The result of this optimization is that many of the elements of the data tend to infinity, so that only a few non-zero weights are available; therefore, irrelevant features are removed from the input data.

The implementation of the algorithm is based on Gaussian Process (GP) machine learning using a zero-mean function and a squared exponential covariance function with ARD.

$$k_f^{ARD}\left(x_p, x_q\right) = \sigma_f^2 \cdot \exp\left[-\frac{1}{2}\sum_{i=1}^{n}\left(\frac{x_p^i - x_q^i}{\sigma_i}\right)^2\right] \tag{12}$$

where σ_i is the covariance function along input feature $i(i = 1, 2, \ldots, n)$ and σ_f is the standard deviation of the signal. Let us suppose that value σ_i is substantial. Then, the covariance function becomes independent of the $i - th$ Input.

The input to ARD in this study was selected from the 280 sets of EIS data collected over 1700 cycles in the second life stage of eight cells, with each EIS profile containing 141 frequency points with fundamental-part and imaginary-part data, as shown in Figure 14. Let us define the weighting factor at the $i-th$ frequency as $w_i = \exp(-\sigma_i)$, $0 < w_i < 1$. The ARD algorithm identifies correlations with the battery health status (capacity) among the high-dimensional impedances at 141 frequency points, assigning the larger weights to features with higher relevance and less weights to the features with lower correlation. The ARD results showing the weights of impedances versus battery capacity at different frequencies are shown in Figure 15. There were nine feature frequencies with weights above 0.01. The locations of these frequency points on the Nyquist plot are shown in Figure 16, with the colored marked points in the plot being where the feature frequencies are located. From the shape of the impedance spectrum curve, the ARD-based feature selection method can select the critical nodes in the impedance spectrum; in other words, together, these feature frequency points can essentially locate the entire EIS curve.

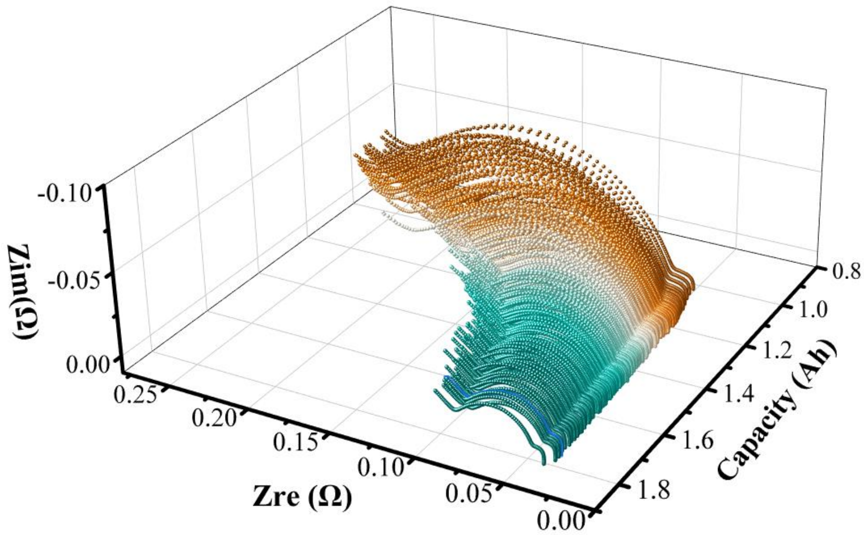

Figure 14. Measured EIS as a function of battery capacity.

As shown in Figures 17 and 18, the following characteristics were applicable to the real and imaginary parts of the impedance values at the characteristic frequencies: (i) The absolute values of the real and imaginary parts of the impedance at all characteristic frequency points increased as the capacity decreased. (ii) At frequencies below 0.1 Hz for the real part/below 1 Hz for the imaginary part, the impedance distribution was more spread out in the lower capacity region, especially for battery capacities below 1.3 Ah (60% of the SOH). This suggested that the features extracted in the lower frequency region were more sensitive to the variability among the retired batteries. (iii) The gradient of impedance variation was more pronounced at frequencies below 0.1 Hz for the real part/below 1 Hz for the imaginary part, but it showed a clear non-linear trend and a relatively scattered distribution. (iv) The impedance distribution at frequencies below 0.1 Hz for the real part/below 1 Hz for the imaginary part was more dispersed in the regions with lower capacity, mainly for battery capacities below 1.3 Ah (60% of the SOH). This suggested that the features extracted in the lower frequency region were more sensitive to the variability among the retired batteries.

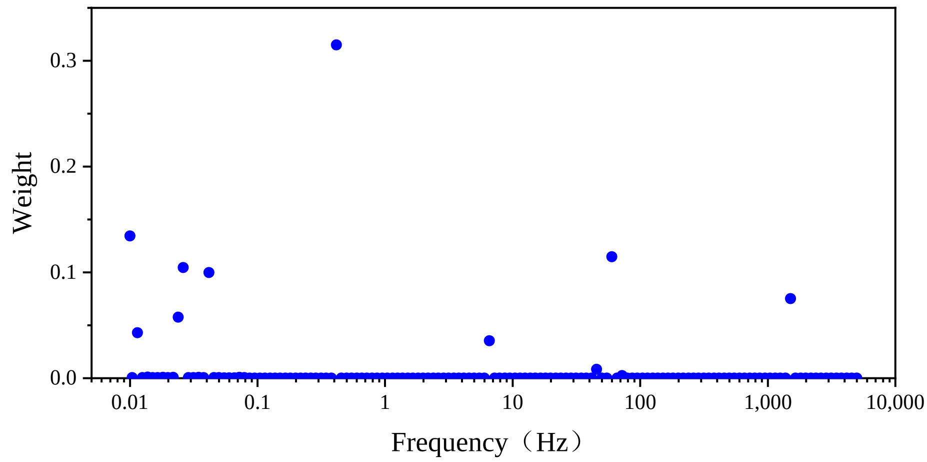

Figure 15. The weighting of impedance vs. battery capacity at different frequencies.

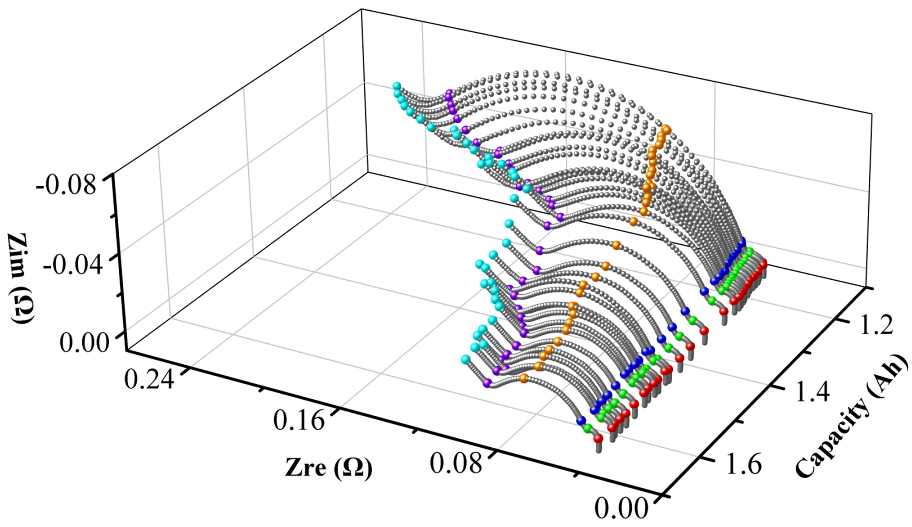

Figure 16. ARD selected eigenfrequencies on Nyquist plot (Cell-1).

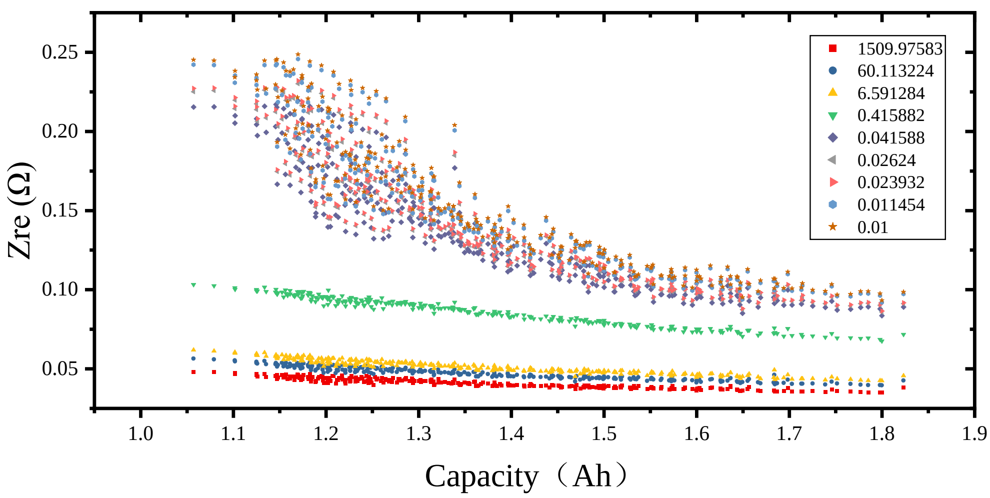

Figure 17. Relationship between the real part of the impedance and the capacity at the characteristic frequency.

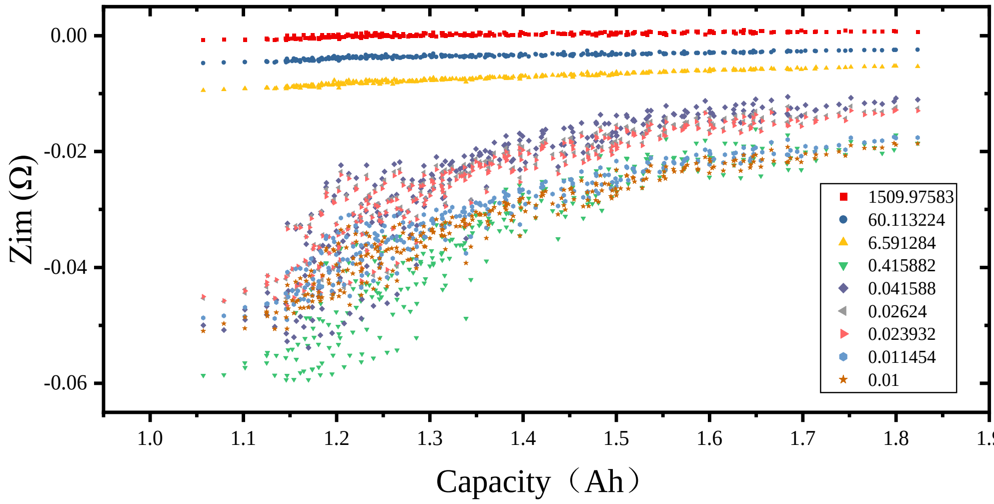

Figure 18. Relationship between the imaginary part of the impedance and the capacity at the characteristic frequency.

4. Case Study

4.1. Verification of SOH Estimation Method Based on EIS

Data-driven methods have been widely studied in the field of fault prediction and health management. Deep learning has the ability to process large numbers of data of complex nonlinear systems without the need for detailed information of known battery characteristics. However, the current traditional deep learning network architecture lacks uncertainty measurement in prediction, which makes it difficult to provide reliable guidance for maintenance decisions in practical engineering applications. The Bayesian neural network introduces the Bayesian method into the construction of deterministic neural networks to quantify the uncertainty [37,38]. This method allows one to quantify the uncertainty of the prediction results through a posterior distribution.

In this paper, the BNN model was constructed and trained using the Tensorflow-Probability probabilistic programming tool in the Python environment, and the main steps were as follows:

- Dataset division using random division, leave-one-out division, and division by a specified number of cycles, respectively, as shown in Table 3.
- Feature set pre-processing—normalization of multi-dimensional features of the input.
- Building a Bayesian neural network and optimizing the network structure: The BNN network structure (number of layers and neurons) was optimally adjusted according to the input; the activation function was ReLU, and the optimizer was Adam. The final BNN model was tested using the dataset to derive the capacity estimation results and the uncertainty.

Overall, 56 cases were trained and tested. This study investigated the performance of the SOH estimation model for retired batteries based on different input features of EIS, training sets, and test sets. Methodologically, these cases were divided into two main categories based on ARD auto-correlation decision feature frequency and ECM parameter identification. Subsequently, three types of data partitioning were used for the above two categories of cases based on the data partitioning method: (i) with random partitioning, we randomly selected one of the eight battery datasets as the test set in order to test the performance of the method on the battery variability dataset; (ii) with leave-one-out partitioning, we used one of the eight battery datasets as the test set in order to test the performance of the method on unknown battery data of the same type; (iii) with division by a specified number of cycles, we used the data from the first N measurements of all batteries as the training set in order to test the performance of the method on unknown battery cycle data. Furthermore, based on the feature quantities, in the case studies, we investigated the performance of the real- and imaginary-part feature quantities in SOH estimation with the ARD method and the performance of different impedance parameters in SOH estimation with the ECM method. The accuracy and generalizability of the model in these cases were discussed explicitly in the comparison of the results and analyses.

Table 3. Examples of BNN model training and validation.

Cases	Method	Data Division	Feature Quantity
1	ARD	Random division (1/8)	All real parts
2			Real part (above 0.1 Hz)
3			Real part (below 0.1 HZ)
4			All the imaginary parts
5			Imaginary part (above 1 Hz)
6			Imaginary part (below 1 Hz)
7			All real and imaginary parts
8			Real part and imaginary part (above 1 Hz)
9–16		Leave-one-out method of division (1/8 Cells)	Real part (above 0.1 Hz)
17–24			Real part (above 1 Hz)
25–31		Divided by cycle numbers (interval, 200)	Real part (above 0.1 Hz)
32–38			Imaginary part (above 1 Hz)
39	ECM	Random division (1/8)	R_O
40			Z_W
41			$[R_O, Z_W]$
42–49		Leave-one-out method of division (1/8 Cells)	$[R_O, Z_W]$
50–56		By cycle numbers (interval, 200)	

4.2. Results of the EIS-Based SOH Estimation Method

Table 4 summarizes model training and testing on the 56 cases in Table 3. With the same data division principle, this section provides a comparative analysis of the model accuracy and generalizability of the different methods.

Table 4. Model test results and errors for different cases.

Case	Method	Data Division	RMASE (Ah)	MAPE (%)
1	ARD	Random division (1/8)	0.178	10.82
2			0.037	2.08
3			0.052	3.00
4			0.183	11.31
5			0.036	1.96
6			0.038	2.29
7			0.337	18.61
8			0.034	1.94
9–16		Leave-one-out method of division (1/8 cells)	[0.027, 0.062]	[1.55, 2.82]
17–24			[0.024, 0.042]	[1.25, 2.35]
25–31		Divided by cycle numbers (interval, 200)	[0.056, 0.408]	[3.81, 27.93]
32–38			[0.038, 0.307]	[2.45, 22.72]
39	ECM	Random division (1/8)	0.0743	4.22
40			0.0407	2.38
41			0.0397	2.27
42–49		Leave-one-out method of division (1/8 cells)	[0.021, 0.050]	[1.38, 2.88]
50–56		By cycle numbers (interval, 200)	[0.052, 0.398]	[3.53, 27.15]

(1) **Random Division**

The model test errors, RMSE and MAPE, for all cases are represented in Figure 19. The training and test results for the ECM-based and ARD-based cases are shown in Figures 20 and 21, respectively. Each subplot in the figure is labeled with a case number corresponding to the cases in Tables 3 and 4. In each case, there are two subplots: the top one is the plot of the training results and errors, and the bottom one is the plot of the test results and errors. In the graphs, the horizontal axis (X-axis) represents the number of samples trained or tested, and the vertical axis (Y-axis) represents the battery capacity. The red line represents the true value of the battery capacity; the blue line represents the estimated value of the battery capacity; and the gray-filled area is the interval estimate (95% confidence interval).

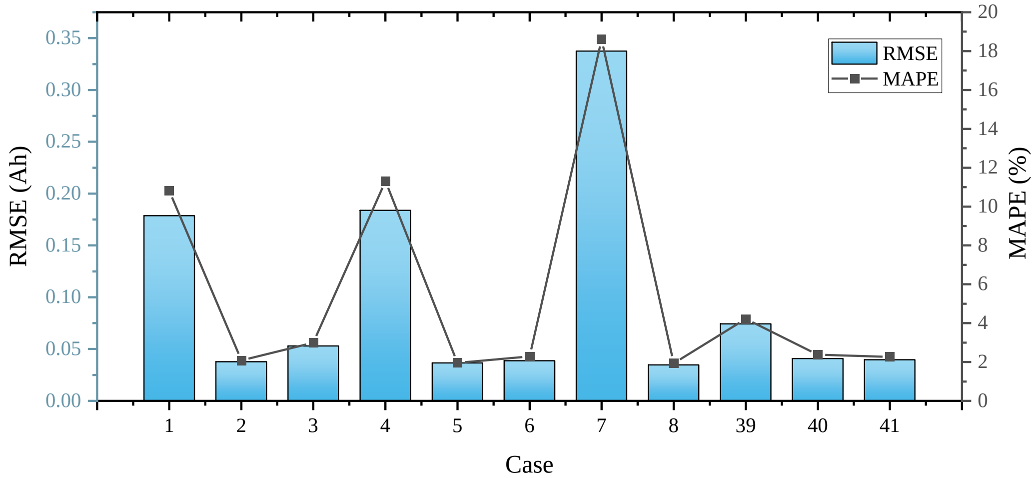

Figure 19. Model test errors based on random division.

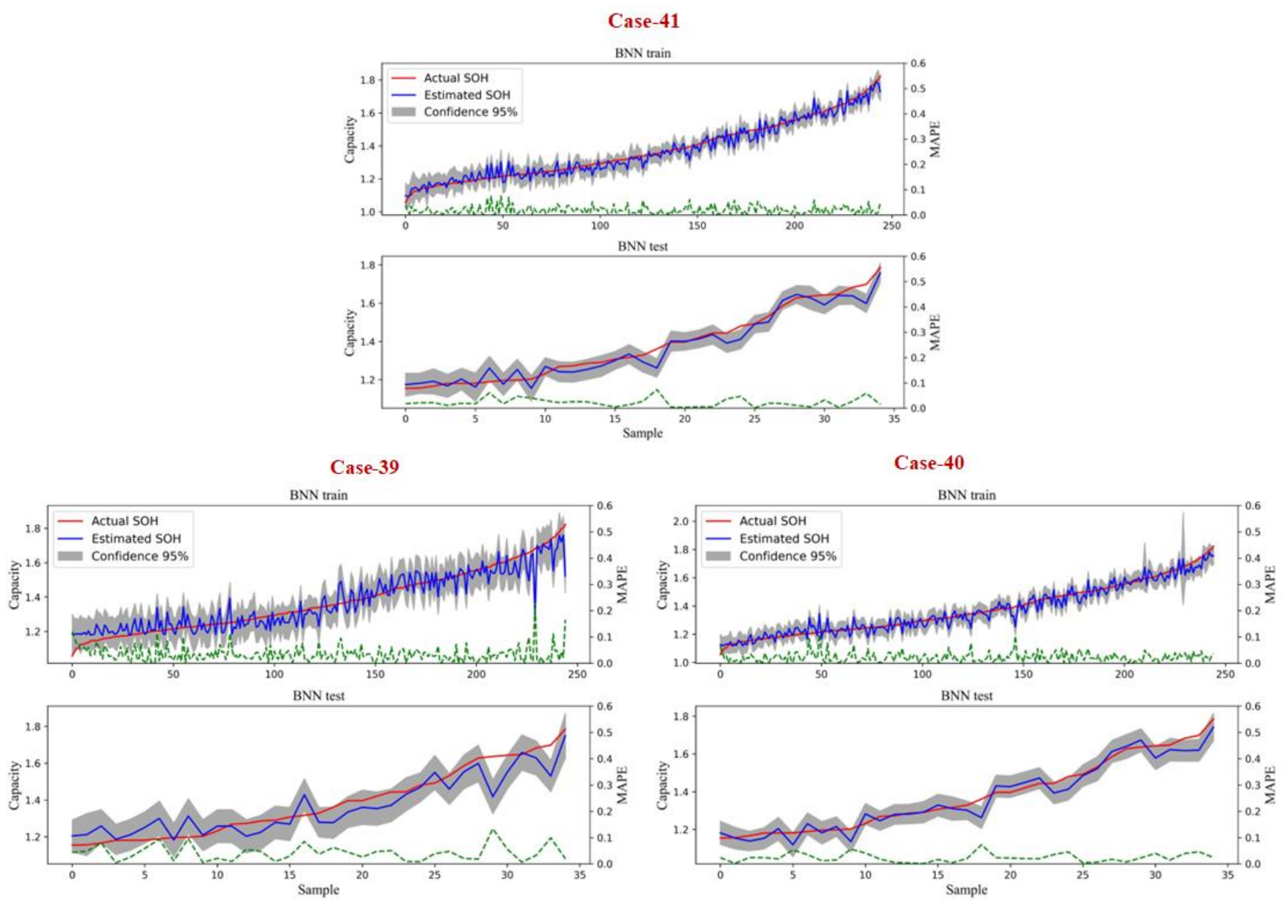

Figure 20. Training and test results of cases based on ECM and random division.

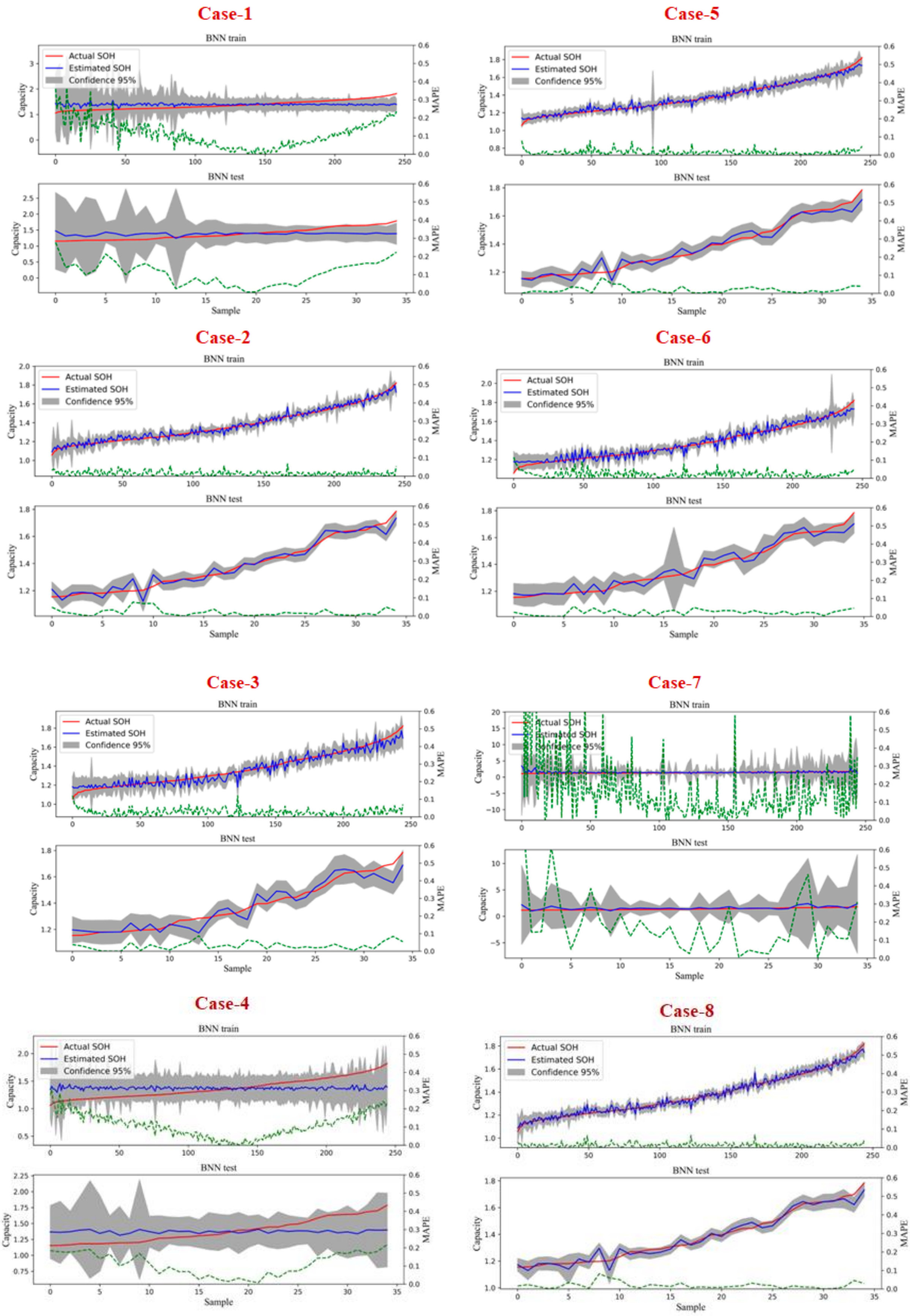

Figure 21. Training and test results of cases based on ARD and random division. Green line: MAPE.

Figures 19 and 20 confirm that the parameters used in the ECM (Case-40) were better than those used in Case-39, which reduced the test error from 4.22% to 2.38%, indicating that the diffuse impedance may be more advantageous in the estimation of the SOH of retired batteries. The accuracy of the model that used both parameters was better than the one that used one source, with a minimum test error of 2.27%.

Regarding the ARD approach, that the following conclusions were drawn:

- Of the three sets of cases (Case-1, Case-2, and Case-3) using the real part of the impedance, the model for Case-1 had the most prominent error in the test set, which indicated that using the eigenfrequencies of all frequency bands was detrimental to the accuracy of the SOH model. The accuracy of the capacity estimation using the high-frequency band of the real-part (above 0.1 Hz) eigenfrequencies was higher than that for the low-frequency band (below 0.1 Hz), which could be attributed to the fact that the real-part values for the high-frequency part of the eigenfrequencies exhibited a different, high degree of nonlinearity and dispersion with respect to the capacity. This shows that the features of the high-frequency band of the real part are more applicable to the estimation of the SOH of retired batteries.
- Of the three sets of cases (Case-4, Case-5, and Case-6) using the real part of the impedance, the model for Case-4 had the largest error in the test set, and Case-5 had the smallest error. The SOH estimation model using the high frequency (1 Hz) and the above eigenfrequencies of the real part had the highest accuracy for reasons similar to those in the analysis of the real part, indicating that the features in the high-frequency band of the imaginary part are more suitable for the estimation of the SOH of retired batteries.
- Of the two sets of cases (Case-7 and Case-8) where both impedance real and imaginary features were used, Case-7, with 18-dimensional features in all frequency bands, had the highest error, while the model accuracy was the highest with real and imaginary features in the high-frequency bands only. This indicates that although features related to battery capacity can be extracted in the low-frequency band of EIS spectra, highly non-linear and high-dimensional features are not conducive to the training of SOH estimation models for retired batteries.
- In terms of the amount of EIS features, good results could be achieved using both the real and imaginary impedance features alone, with test errors of 2.08% and 1.96%, respectively. Combining the real and imaginary impedance features did not significantly improve the accuracy of the model, with a minimum test error of 1.94%.

Combining the above analyses, the best cell SOH estimation accuracy achieved by the ARD-based method was 1.94%, and the best cell SOH estimation accuracy achieved by the ECM-based method was 2.27%. Therefore, considering the results of the random division experiment, the ARD-based method was slightly better than the ECM-based method in terms of SOH estimation accuracy.

(2) **Leave-one-out method of division**

The test errors of the BNN models with different features using leave-one-out division are shown in the box line plot in Figure 22, where the RMSE is reported on the left Y-axis (red) and the MPAE on the right Y-axis (blue). The best and worst model training and test results for the three features are given in Figures 23–25, respectively, with the lowest test error being on the left and the cell numbers being the cell numbers of the test set. Figures 23 and 24 show the test results of the model training set with the impedance real-part and imaginary-part features based on the ARD method, respectively, and Figure 25 shows the model training and test results based on the ECM method. The training and test results based on leave-one-out method division revealed the following:

- Figures 22 and 23 show that the MAPE range of test errors based on the real part of the ARD impedance (Zre) was [1.55, 2.82], indicating a large inter-cell variability for this feature. The lowest BNN model test error was obtained for Cell-3, and the most significant error was obtained for Cell-5. As seen from Figures 5–13, some of the actual capacity of Cell-5 exceeded the BNN model interval estimate, mainly because the model had a higher estimation error near the inflection point of the capacity.

- From Figures 22 and 24, the test errors based on the ARD impedance imaginary part (Zim) were relatively close to each other, with a range of [1.25, 2.35] for the MAPE, which indicated that the impedance imaginary-part characteristics were less affected by inter-cell capacity variability, with the lowest model test error having been obtained for Cell-1 and the largest error having been obtained for Cell-7. In addition, the comparison of the median and maximum error values showed that the BNN model with the ARD impedance imaginary part was the best performing one out of the three methods.
- From Figures 22 and 25, the range of MAPE test errors based on the ECM method was [1.38, 2.88]; the maximum error was the highest for the three characteristics, and the error range was also the largest, which reflected that the parameters of the ECM were more significantly influenced by inter-cell variability. As can be seen from Figure 25, using the BNN model, the lowest error was obtained for Cell-8, and the biggest error was obtained for Cell-5. These results were similar to the results obtained by utilizing the real part of the ARD impedance characteristics, where the test results for Cell-5 had a bigger estimation error around the changing point of the capacity.

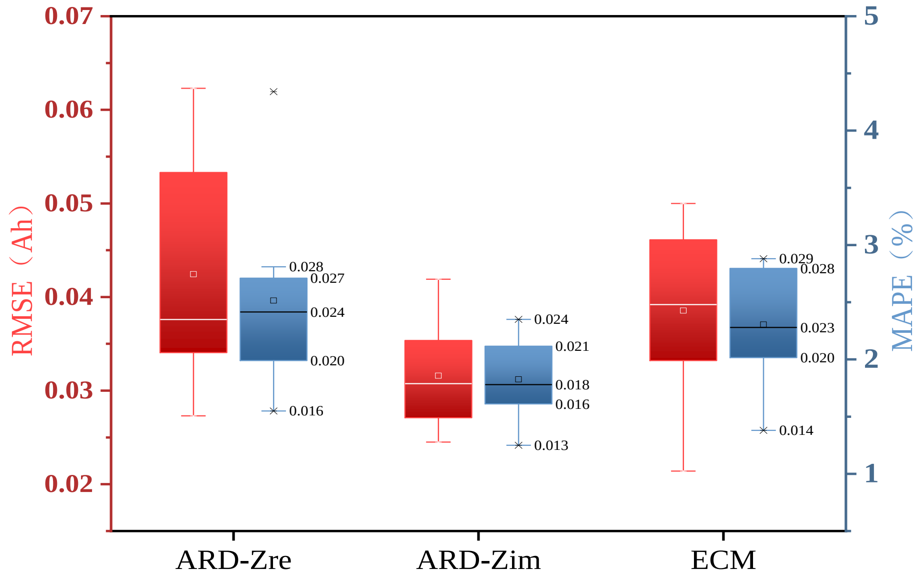

Figure 22. Error distribution of results for the model using leave-one-out division.

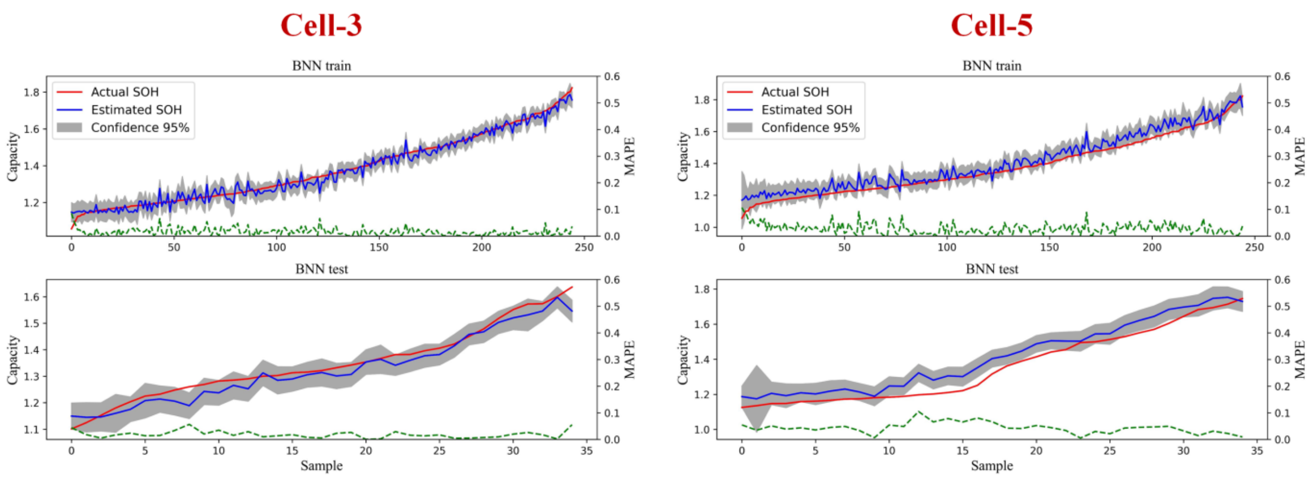

Figure 23. Validation of ARD-based impedance real-part feature using leave-one-out method/ Green line: MAPE.

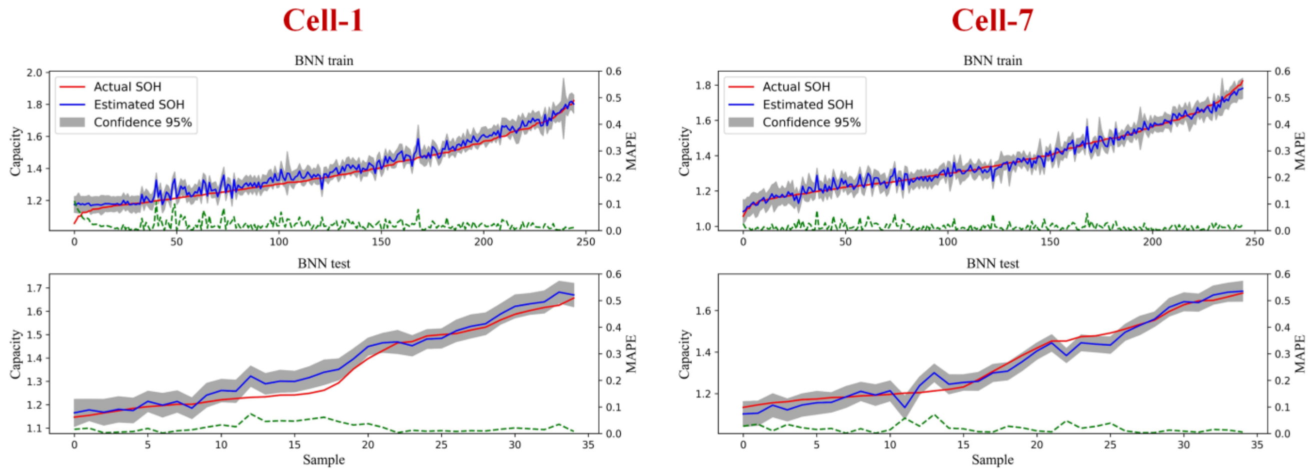

Figure 24. The impedance imaginary-part feature/ Green line: MAPE.

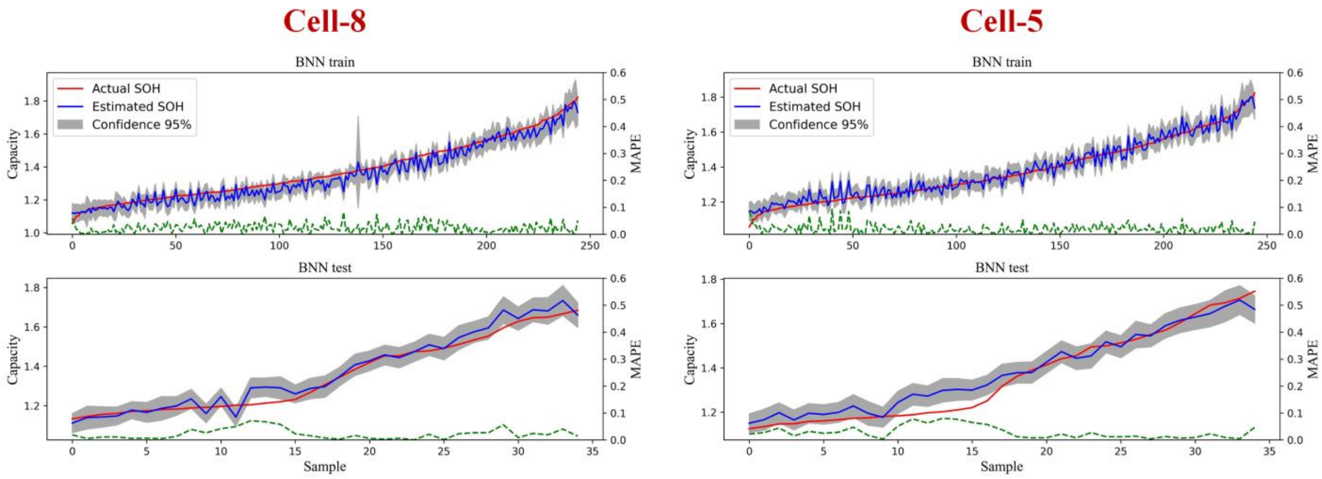

Figure 25. Validation of the leave-one-out method based on the ECM method/ Green line: MAPE.

(3) **Specifying the number of cycles to be divided**

The variations in the model test result errors on the number of cycles in the training set in the ARD-based and ECM-based cases using the principle of leave-one-out division are shown in Figure 26.

The horizontal axis (X-axis) in Figure 26 represents the data from the first *N* cycles of the retired battery contained in the test set, and the vertical axis (Y-axis) shows the RMSE and MAPE, for the remaining data in the test set. The black line represents the test errors based on the impedance imaginary-part feature selected using ARD, and the blue line represents the errors based on the ECM parameter feature. Based on the comparative analysis of the model errors in Figure 26, that the following conclusions were drawn:

- In terms of the number of cycles, as the increase of data amount, both methods showed an abrupt drop in the test error at 600 cycles. This indicated that the best accuracy of capacity estimation can be reached at 2.79%, when the data from the first 600 cycles of the retired battery can be obtained.
- From the comparison of the methods, the test error of the ECM-based method (2.79%) was much smaller than that of the ARD-based method (6.24%) when specifying the first 600 cycles of data as the training set. This indicates that the ECM method has higher accuracy in SOH estimation when the cell cycle data are unknown.

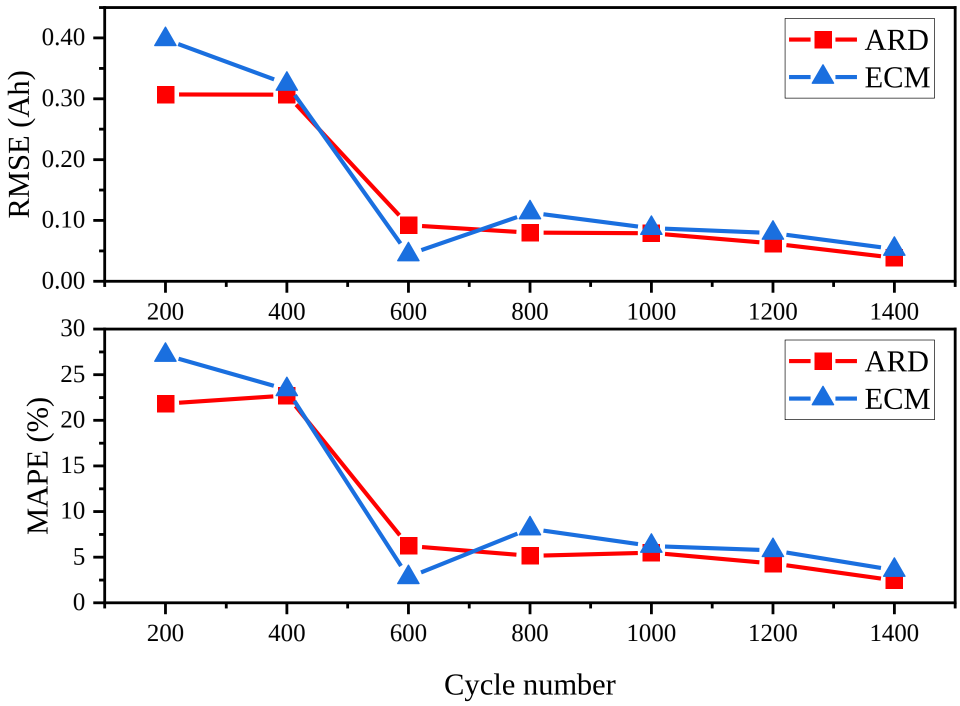

Figure 26. Model test error for the specified number of cycle divisions.

Figure 27 shows the training and test results of the model specifying the first 600 cycles of data as the training set. The estimates from model training were generally able to get very close to the true battery capacity. From the test results of the model, the point estimate still approximated the true battery capacity relatively well as the capacity decreased. However, the 95% confidence interval shown in the figure became significantly more wider, indicating an increase in the uncertainty of capacity estimation. This increase of uncertainty is mainly due to the fact that BNN model training did not consider the data characteristics of the battery at low capacity. In combination, the ECM-based approach is expected to achieve higher accuracy (less than 3% error) in capacity estimation over thousands of subsequent cycles of a retired battery in a case experiment with a specified number of cycles, when the data from the first 600 cycles of the retired battery are obtained.

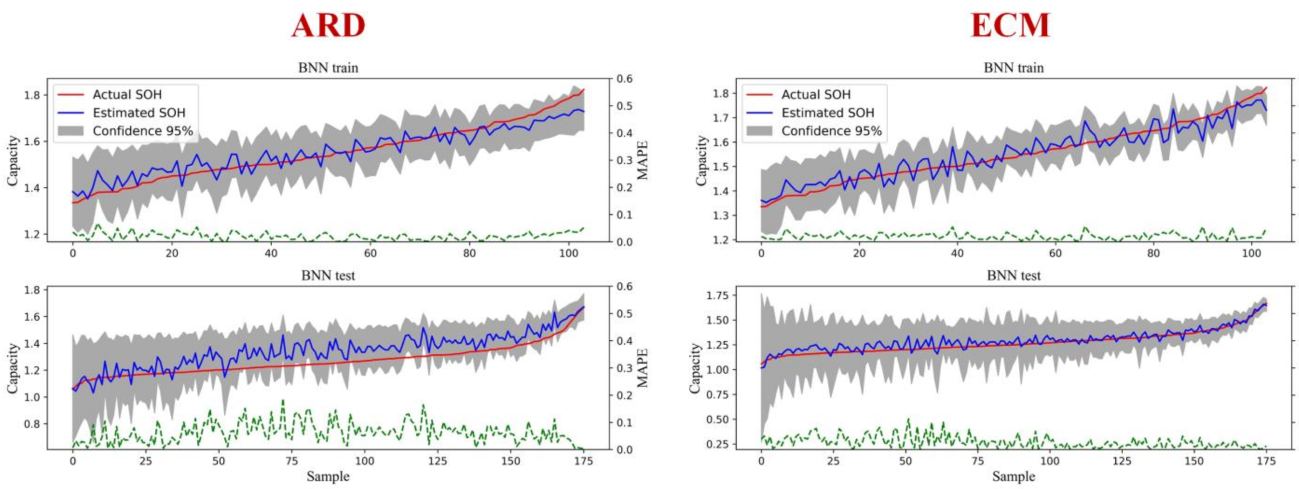

Figure 27. Model results for specifying the first 600 cycles as training data.

4.3. Comparative Analysis of SOH Estimation Methods

The accuracy and generalization performance of the EIS-based method for SOH estimation under various test conditions was compared with that of the Constant Current–

Constant Voltage (CC-CV) charging I-V curve-based method, where all methods were trained and tested on a self-tested dataset. The comparative analysis was carried out using two data division methods, that is, random division, and leave-one-out division.

As shown in Figure 28, the EIS-based method significantly outperformed the CC-CV charging I-V curve-based method in training and testing the model accuracy under the premise of random division. The data-driven method by using the EIS data and ARD method had the highest SOH estimation accuracy, with a training error of 1.39% and a test error of 1.94%. On the other hand, the CC-CV method had a training error of 2.52% and a test error of 3.05%. The comparison showed that the EIS-based method improved the SOH estimation accuracy by 1.11% over the CC-CV-based method.

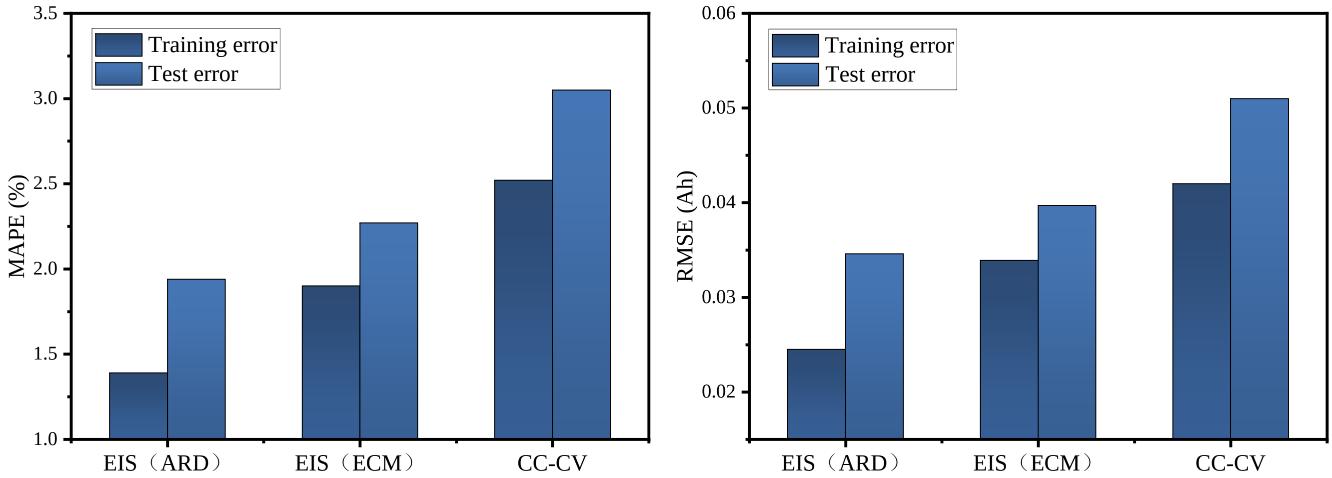

Figure 28. Error comparison of methods using random division.

As shown in Figure 29, the accuracy and generalization performance of the EIS (ARD)-based method was the best in terms of both the training error and the test error, while the CC-CV charging I-V curve-based method performed the worst in terms of accuracy and generalization performance, given the premise of leave-one-out method division. This showed that the EIS-and-ARD-based data-driven method had the best SOH estimation performance on unknown cells of the same type and could overcome the effects of inter-cell inconsistency well, with an overall test error of less than 2%. The CC-CV method was more affected by inter-cell inconsistency but still had an overall test error of less than 4%. The comparison showed that the EIS-based method improved the SOH estimation accuracy by about 2% over the CC-CV-based method.

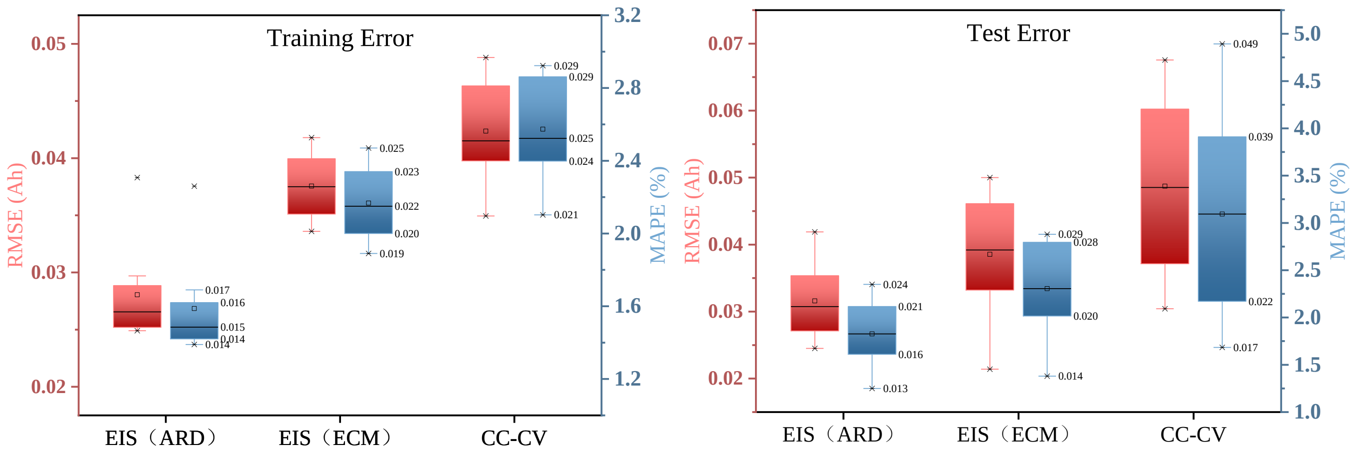

Figure 29. Error comparison of methods using the leave-one-out division.

As shown in Figure 30, with specified cycle division, the three methods showed roughly uniform change patterns with the increase in the number of cycles of the training set, with 600 cycles being the inflection point at which the training and test errors were significantly reduced. Therefore, the method in this paper is expected to achieve better SOH estimation during subsequent battery operation when only the first 600 cycles of retired battery data are obtained. Regarding the training error, the ARD-based method had the highest accuracy, while the CC-CV-based method had the lowest accuracy. In terms of the test error, the ECM-based method had the best generalization performance on the test set at 600 cycles.

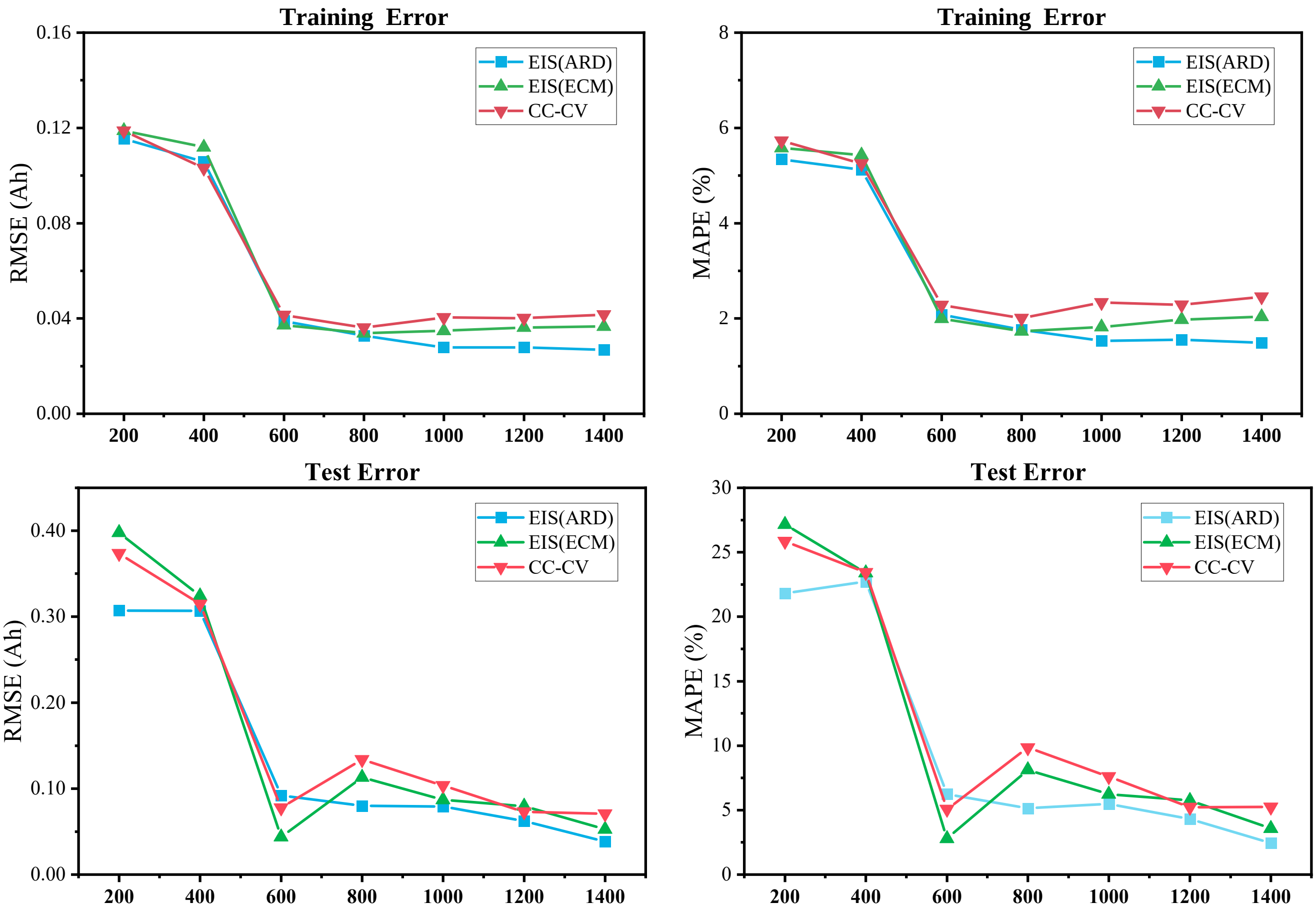

Figure 30. Error comparison of methods using specified cycle division.

In summary, overall, the EIS-based approach significantly outperforms the CC-CV charging I-V curve-based approach in terms of SOH estimation accuracy and generalization performance. Of the two approaches to EIS, the ARD-based data-driven approach outperforms the ECM-based model-driven approach, but the ECM-based approach has the best generalization performance on the test set when only partial cyclic data are available.

5. Conclusions

This paper characterized the aging properties and assessed the state of health (SOH) of retired batteries according to the electrochemical impedance spectroscopy (EIS) technique, for which a battery aging experiment was designed to monitor the aging process of batteries. This study constructed an equivalent circuit model (ECM) for retired batteries and identified the correlation between ECM parameters and aging batteries. Moreover, a Bayesian neural network-based SOH estimation method with automatic feature extraction was developed. The conclusions of this paper are as follows: (i) The impedance variables at high frequencies of EIS are highly non-linear with respect to the SOH and are affected by battery inconsistency in the low-capacity region, while they are linear with respect to the SOH at low frequencies. (ii) The SOH estimation error is less than 2% and better than several existing methods. (iii) The ECM-based method holds higher accuracy (less than 3% error) in SOH estimation.

This paper fully verified that in a retired battery BMS system, EIS detection can provide abundant information about the inside of the battery, including electrochemical reactions, which can help to improve the estimation accuracy of the battery SOH.

Author Contributions: Conceptualization, Z.X. and K.O.; methodology, Z.X., H.L. and K.O.; validation, M.Y., K.O. and W.P.; formal analysis, Z.X. and K.O.; writing—original draft preparation, Z.X., H.L. and M.Y.; writing—review and editing, K.O. and W.P.; visualization, Z.X. and K.O.; supervision, W.P.; funding acquisition, H.L. and W.P. All authors have read and agreed to the published version of the manuscript.

Funding: This work was supported by the National Key R&D Program of China (project No. 2019YFB1704702), Shenzhen Fundamental Research Program (project No. JCYJ20190807155203586), Postdoctoral Research Foundation of China (project No. 2021M703686), Guangdong Basic and Applied Basic Research Foundation (2021A1515110306), and Fundamental Research Funds for the Central Universities, Sun Yat-sen University (project Nos. 22qntd1706 and 22qntd1711).

Data Availability Statement: Data can be accessed by contacting the corresponding author.

Conflicts of Interest: The authors declare no conflict of interest.

Abbreviations

State of health	SOH
electrochemical impedance spectroscopy	EIS
Equivalent circuit model	ECM
Pseudo Two-Dimensional	P2D
Single-Particle Model	SPM
state of charge	SOC
Maximum Rechargeable Capacity	MRC
Maximum Dischargeable Capacity	MDC
Depth of discharge	DOD
Solid electrolyte interphase	SEI
Automatic relevance determination	ARD
Constant Current–Constant Voltage	CC-CV

References

1. Kennedy, B.; Patterson, D.; Camilleri, S. Use of lithium-ion batteries in electric vehicles. *J. Power Sources* **2000**, *90*, 156–162. [CrossRef]
2. Wu, Y.; Yang, L.; Tian, X.; Li, Y.; Zuo, T. Temporal and spatial analysis for end-of-life power batteries from electric vehicles in China. *Resour. Conserv. Recycl.* **2020**, *155*, 104651. [CrossRef]
3. Chen, W.; Liang, J.; Yang, Z.; Li, G. A review of lithium-ion battery for electric vehicle applications and beyond. *Energy Procedia* **2019**, *158*, 4363–4368. [CrossRef]
4. Zhang, Q.; Li, X.; Du, Z.; Liao, Q. Aging performance characterization and state-of-health assessment of retired lithium-ion battery modules. *J. Energy Storage* **2021**, *40*, 102743. [CrossRef]
5. Li, J.; Gu, Y.; Wang, L.; Wu, X. Review on state of health estimation of retired lithium-ion batteries. *Energy Storage Sci. Technol.* **2019**, *8*, 807.
6. Iurilli, P.; Brivio, C.; Wood, V. On the use of electrochemical impedance spectroscopy to characterize and model the aging phenomena of lithium-ion batteries: A critical review. *J. Power Sources* **2021**, *505*, 229860. [CrossRef]
7. Xiong, R.; Li, L.; Tian, J. Towards a smarter battery management system: A critical review on battery state of health monitoring methods. *J. Power Sources* **2018**, *405*, 18–29. [CrossRef]
8. Li, H.; Díaz, H.; Soares, C.G. A failure analysis of floating offshore wind turbines using AHP-FMEA methodology. *Ocean. Eng.* **2021**, *234*, 109261. [CrossRef]
9. Li, H.; Soares, C.G.; Huang, H.Z. Reliability analysis of a floating offshore wind turbine using Bayesian Networks. *Ocean. Eng.* **2020**, *217*, 107827. [CrossRef]
10. Li, H.; Huang, C.G.; Soares, C.G. A real-time inspection and opportunistic maintenance strategies for floating offshore wind turbines. *Ocean. Eng.* **2022**, *256*, 111433. [CrossRef]
11. Li, H.; Soares, C.G. Assessment of failure rates and reliability of floating offshore wind turbines. *Reliab. Eng. Syst. Saf.* **2022**, *228*, 108777. [CrossRef]

12. Li, H.; Yazdi, M. *Advanced Decision-Making Methods and Applications in System Safety and Reliability Problems: Approaches, Case Studies, Multi-Criteria Decision-Making, Multi-Objective Decision-Making, Fuzzy Risk-Based Models*; Springer Nature: Cham, Switzerland, 2022; Volume 211.
13. Dees, D.; Gunen, E.; Abraham, D.; Jansen, A.; Prakash, J. Electrochemical modeling of lithium-ion positive electrodes during hybrid pulse power characterization tests. *J. Electrochem. Soc.* **2008**, *155*, A603. [CrossRef]
14. Ren, H.; Zhao, Y.; Chen, S.; Wang, T. Design and implementation of a battery management system with active charge balance based on the SOC and SOH online estimation. *Energy* **2019**, *166*, 908–917. [CrossRef]
15. Fu, Y.; Xu, J.; Shi, M.; Mei, X. A fast impedance calculation-based battery state-of-health estimation method. *IEEE Trans. Ind. Electron.* **2021**, *69*, 7019–7028. [CrossRef]
16. Li, W.; Cao, D.; Jöst, D.; Ringbeck, F.; Kuipers, M.; Frie, F.; Sauer, D.U. Parameter sensitivity analysis of electrochemical model-based battery management systems for lithium-ion batteries. *Appl. Energy* **2020**, *269*, 115104. [CrossRef]
17. Pramanik, S.; Anwar, S. Electrochemical model based charge optimization for lithium-ion batteries. *J. Power Sources* **2016**, *313*, 164–177. [CrossRef]
18. Jokar, A.; Rajabloo, B.; Désilets, M.; Lacroix, M. Review of simplified Pseudo-two-Dimensional models of lithium-ion batteries. *J. Power Sources* **2016**, *327*, 44–55. [CrossRef]
19. Gandomi, Y.A.; Zawodzinski, T.A.; Mench, M.M. Concentrated solution model of transport in all vanadium redox flow battery membrane separator. *ECS Trans.* **2014**, *61*, 23. [CrossRef]
20. Guo, M.; Sikha, G.; White, R.E. Single-particle model for a lithium-ion cell: Thermal behavior. *J. Electrochem. Soc.* **2010**, *158*, A122. [CrossRef]
21. Tran, M.K.; Mevawala, A.; Panchal, S.; Raahemifar, K.; Fowler, M.; Fraser, R. Effect of integrating the hysteresis component to the equivalent circuit model of Lithium-ion battery for dynamic and non-dynamic applications. *J. Energy Storage* **2020**, *32*, 101785. [CrossRef]
22. Zhang, X.; Lu, J.; Yuan, S.; Yang, J.; Zhou, X. A novel method for identification of lithium-ion battery equivalent circuit model parameters considering electrochemical properties. *J. Power Sources* **2017**, *345*, 21–29. [CrossRef]
23. Chang, B.Y.; Park, S.M. Electrochemical impedance spectroscopy. *Annu. Rev. Chem.* **2010**, *3*, 207. [CrossRef] [PubMed]
24. Li, J.; Castellazzi, A.; Eleffendi, M.A.; Gurpinar, E.; Johnson, C.M.; Mills, L. A physical RC network model for electrothermal analysis of a multichip SiC power module. *IEEE Trans. Power Electron.* **2017**, *33*, 2494–2508. [CrossRef]
25. Kapetanios, G.; Shin, Y.; Snell, A. Testing for cointegration in nonlinear smooth transition error correction models. *Econom. Theory* **2006**, *22*, 279–303. [CrossRef]
26. He, H.; Xiong, R.; Zhang, X.; Sun, F.; Fan, J. State-of-charge estimation of the lithium-ion battery using an adaptive extended Kalman filter based on an improved Thevenin model. *IEEE Trans. Veh. Technol.* **2011**, *60*, 1461–1469.
27. Jiang, N.; Pang, H. Study on Co-estimation of SoC and SoH for second-use lithium-ion power batteries. *Electronics* **2022**, *11*, 1789. [CrossRef]
28. Pang, B.; Chen, L.; Dong, Z. Data-driven degradation modeling and SOH prediction of Li-ion batteries. *Energies* **2022**, *15*, 5580. [CrossRef]
29. Oji, T.; Zhou, Y.; Ci, S.; Kang, F.; Chen, X.; Liu, X. Data-driven methods for battery soh estimation: Survey and a critical analysis. *IEEE Access* **2021**, *9*, 126903–126916. [CrossRef]
30. Suykens, J.A.; Vandewalle, J. Least squares support vector machine classifiers. *Neural Processing Lett.* **1999**, *9*, 293–300. [CrossRef]
31. Retter, U.; Lohse, H. Electrochemical impedance spectroscopy. In *Electroanalytical Methods*; Springer: Berlin/Heidelberg, Germany, 2010; pp. 159–177.
32. Ragoisha, G.A.; Bondarenko, A.S. Potentiodynamic electrochemical impedance spectroscopy. *Electrochim. Acta* **2005**, *50*, 1553–1563. [CrossRef]
33. Randviir, E.P.; Banks, C.E. Electrochemical impedance spectroscopy: An overview of bioanalytical applications. *Anal. Methods* **2013**, *5*, 1098–1115. [CrossRef]
34. Ciucci, F. Modeling electrochemical impedance spectroscopy. *Curr. Opin. Electrochem.* **2019**, *13*, 132–139. [CrossRef]
35. Liu, J.; Wan, T.H.; Ciucci, F. A Bayesian view on the Hilbert transform and the Kramers-Kronig transform of electrochemical impedance data: Probabilistic estimates and quality scores. *Electrochim. Acta* **2020**, *357*, 136864. [CrossRef]
36. Qi, Y.; Minka, T.P.; Picard, R.W.; Ghahramani, Z. Predictive automatic relevance determination by expectation propagation. In Proceedings of the Twenty-First International Conference on Machine Learning (2004), Banff, AB, Canada, 4–8 July 2004; p. 85.
37. Peng, W.; Ye, Z.-S.; Chen, N. Bayesian deep-learning-based health prognostics toward prognostics uncertainty. *IEEE Trans. Ind. Electron.* **2019**, *67*, 2283–2293. [CrossRef]
38. Kwon, Y.; Won, J.H.; Kim, B.J.; Paik, M.C. Uncertainty quantification using Bayesian neural networks in classification: Application to biomedical image segmentation. *Comput. Stat. Data Anal.* **2020**, *142*, 106816. [CrossRef]